

Nuclear F-actin and myosins drive relocalization of heterochromatic breaks

Christopher P. Caridi^{1,3}, Carla D'Agostino^{1,3}, Taehyun Ryu¹, Grzegorz Zapotoczny¹, Laetitia Delabaere¹, Xiao Li¹, Varandt Y. Khodaverdian¹, Nuno Amaral^{1,2}, Emily Lin¹, Alesandra R. Rau¹ & Irene Chiolo^{1*}

Heterochromatin mainly comprises repeated DNA sequences that are prone to ectopic recombination. In *Drosophila* cells, 'safe' repair of heterochromatic double-strand breaks by homologous recombination relies on the relocalization of repair sites to the nuclear periphery before strand invasion. The mechanisms responsible for this movement were unknown. Here we show that relocalization occurs by directed motion along nuclear actin filaments assembled at repair sites by the Arp2/3 complex. Relocalization requires nuclear myosins associated with the heterochromatin repair complex Smc5/6 and the myosin activator Unc45, which is recruited to repair sites by Smc5/6. ARP2/3, actin nucleation and myosins also relocalize heterochromatic double-strand breaks in mouse cells. Defects in this pathway result in impaired heterochromatin repair and chromosome rearrangements. These findings identify de novo nuclear actin filaments and myosins as effectors of chromatin dynamics for heterochromatin repair and stability in multicellular eukaryotes.

Specialized mechanisms promote repair by homologous recombination in pericentromeric heterochromatin (hereafter, heterochromatin) while preventing aberrant recombination^{1,2}. Heterochromatin constitutes about 30% of fly and human genomes³, mostly comprising repeated DNA sequences (for example, transposons and satellite repeats⁴) and 'silent' epigenetic marks³ (such as dimethylation or trimethylation of histone H3 at lysine 9 (H3K9me2/3) and heterochromatin protein 1 (HP1)), but is absent in budding yeast. In heterochromatin, thousands to millions of identical sequences, even from different chromosomes, can engage in ectopic recombination, presenting a serious threat to genome stability in multicellular eukaryotes^{1,2,5–8}.

In Drosophila melanogaster, heterochromatin forms a distinct nuclear domain^{5,9}, and aberrant recombination is prevented by relocalization of double-strand breaks (DSBs) to the nuclear periphery before Rad51 recruitment^{5-8,10}. Loss of components required for relocalization (such as dPIAS SUMO E3-ligase, or the Smc5/6 SUMO E3-ligase subunits (called Qit and Cerv in Drosophila and are both Nse2 homologues)) or for anchoring to the periphery (such as the nuclear pore protein Nup107 or the inner nuclear membrane proteins Koi and Spag4) results in defects in heterochromatin repair and widespread chromosome rearrangements^{5,7,8}. Relocalization is likely to prevent aberrant recombination by separating damaged DNAs from similar repeats on non-homologous chromosomes, while promoting 'safe' exchanges with the sister chromosome or homologue 1,2,5-8. A similar relocalization to outside heterochromatic 'chromocentres' occurs during homologous recombination in mouse cells in the G2 phase of the cell cycle^{6,11,12}. The mechanisms that drive this notable movement remain to be identified.

Actin nucleators drive DSB relocalization

Nuclear actin filaments (F-actin) form in response to DSBs in mammalian cells and have poorly understood functions in repair $^{13-15}$. We tested the role of actin polymerization in relocalization of heterochromatic DSBs. In *Drosophila* cells, repair sites start to leave the heterochromatin domain 10 min after the induction of DSBs with ionizing radiation (IR), resulting in a decrease in repair sites (γ H2Av foci) in

DAPI-bright heterochromatin and an increase at the nuclear periphery 60 min after IR^{5,7}. Inhibition of actin polymerization with latrunculin B (LatB) increases the number of γ H2Av foci in DAPI-bright heterochromatin 60 min after IR, without affecting the total number of foci (Extended Data Fig. 1a). Similarly, activation of the Arp2/3 actin nucleator by RNA interference (RNAi) or CK666 treatment results in more foci remaining in DAPI-bright heterochromatin and fewer reaching the nuclear periphery, consistent with relocalization defects (Fig. 1a, Extended Data Fig. 1b-e). Removal of LatB or CK666 reverses the effects (Extended Data Fig. 1f, g), ruling out permanent damage to repair pathways. RNAi of the actin nucleators Spire and Dia does not affect relocalization, revealing a specific role of Arp2/3 (Extended Data Fig. 1h). The kinetics of relocalization are comparable in mouse cells, and are similarly affected by ARP3 RNAi or treatment with LatB or CK666 (Fig. 1b, Extended Data Fig. 1i-k), suggesting that relocalization pathways are conserved.

Arp2/3 is activated by the Wiskott–Aldrich syndrome protein family (Wash, Scar, Whamy and Wasp in *Drosophila*). Depletion of Wash or Scar, but not of Whamy or Wasp, causes relocalization defects (Fig. 1c, Extended Data Fig. 1l). Depletion of Arp2/3 alone, Scar and Wash together, or Arp2/3, Scar and Wash together, results in similar relocalization defects, whereas depletion of Scar or Wash alone results in an intermediate phenotype (Fig. 1c), suggesting that Scar and Wash independently activate Arp2/3 for relocalization. Arp2/3 is not required for early repair steps (formation of foci containing Mdc1 (also known as Mu2 in *Drosophila*), Atrip (also known as mus304), Smc6 or Nse2, or suppression of Rad51 foci inside the heterochromatin domain^{5,7,8}; Extended Data Fig. 2a–c), suggesting that actin nucleation mediates relocalization after resection and recruitment of the Smc5/6 complex.

Epistatic analyses place Smc5/6 and Arp2/3 in the same pathway for relocalization (Fig. 1d, Extended Data Fig. 2e), and Arp2/3 co-immunoprecipitates with the Smc5/6 complex in response to IR (Fig. 1e, Extended Data Fig. 2f), suggesting that Arp2/3 has a direct role in heterochromatin repair. Accordingly, Arp2/3 is enriched at repair foci in DAPI-bright heterochromatin 10 min after IR (before relocalization^{5,7}), and most Arp2/3-containing foci colocalize with the

¹Department of Molecular and Computational Biology, University of Southern California, Los Angeles, CA, USA. ²Present address: Karolinska Institute, Stockholm, Sweden. ³These authors contributed equally: Christopher P. Caridi, Carla D'Agostino. *e-mail: chiolo@usc.edu

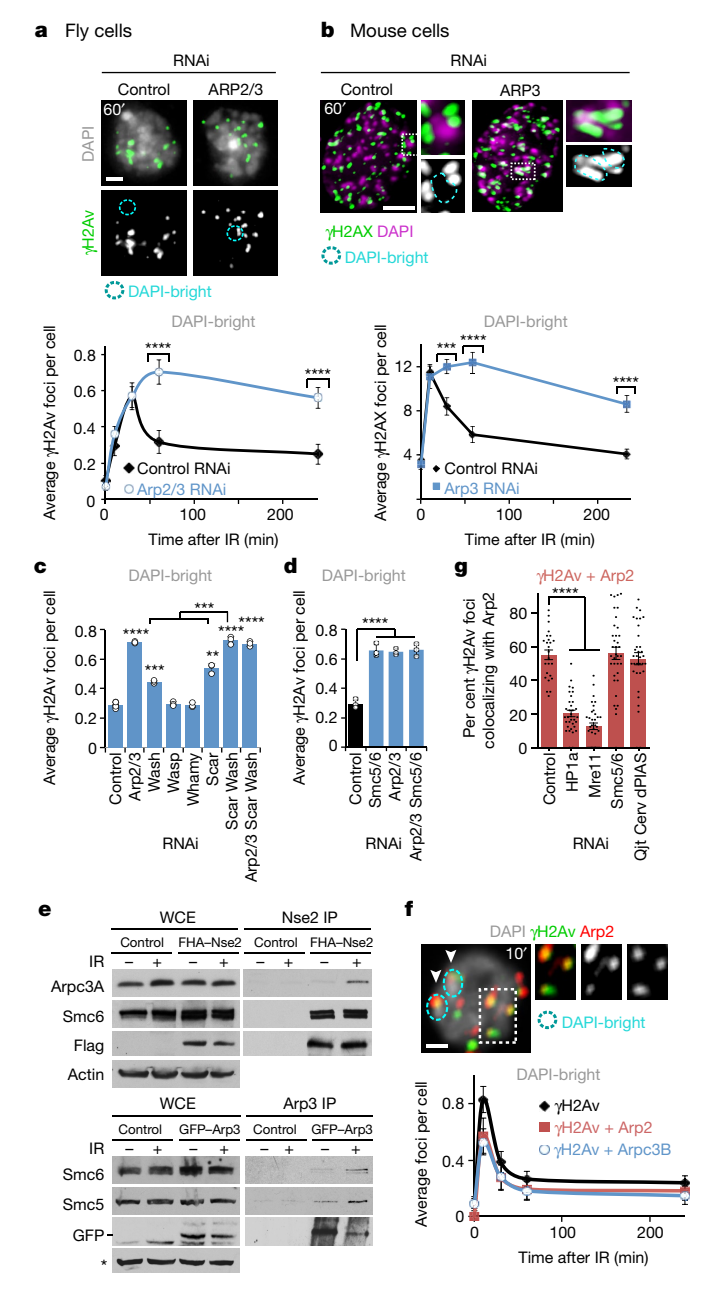


Fig. 1 | Actin nucleators mediate relocalization of heterochromatic **DSBs. a**, Immunofluorescence and quantification of γ H2Av foci in Kc fly cells fixed at indicated time points after IR show γH2Av foci in DAPIbright heterochromatin following indicated RNAi. **** $P \le 0.0001$, $n \ge 100$ cells per RNAi per time point. **b**, As in **a**, except NIH3T3 G2 (PH3-positive) cells were used and γH2AX foci associated with DAPIbright chromocentres were quantified. ****P < 0.0001, ***P = 0.0004, $n \ge 20$ cells per RNAi per time point. c, As in a, with immunofluorescence performed 60 min after IR. ****P < 0.0001, *** $P \le 0.0009$ versus control or as indicated, **P = 0.0019, n > 250 cells per RNAi. **d**, As in **c**; ****P < 0.0001, n > 250 cells per RNAi. **e**, Immunoprecipitation (IP) of FHA-Nse2 or GFP-Arp3 in Kc cells before (-) or after (+) IR and western blot analysis with indicated antibodies. Actin and background band (*) are loading controls. WCE, whole-cell extract. f, Immunofluorescence and quantification of γ H2Av foci colocalizing with FHA(Flag-HA)-Arp2 or Arpc3B in DAPI-bright heterochromatin at indicated time points after IR. Arrowheads show colocalizations in DAPI-bright heterochromatin. n > 30Kc cells per time point per experiment. g, As in f, showing colocalization of γH2Av and Arp2 10 min after IR, following indicated RNAi. *P < 0.0001, n > 22 cells per RNAi. Scale bars, 1 μ m in **a**, **f** and 5 μ m in **b**. Data shown as mean \pm s.e.m. in **a**, **b**, **f**, **g** and mean \pm s.d. of at least three independent experiments in c, d. Headings above each graph indicate the compartments to which quantifications refer. P values calculated with

two-tailed Mann-Whitney test.

heterochromatin mark H3K9me3 (Fig. 1f, Extended Data Fig. 2d, g, h). The Smc5/6 complex, or Smc5/6-dependent SUMOylation, might promote activation of Arp2/3 or its recruitment to DSBs. However, RNAi of Smc5/6 or SUMO E3-ligases does not affect recruitment of Arp2/3 to foci (Fig. 1g), suggesting a role for Smc5/6 in the regulation of Arp2/3. Recruitment of Arp2/3 to repair foci depends on the DSB signalling protein Mre11 and the heterochromatin component HP1a (Fig. 1g, Extended Data Fig. 2i), suggesting that the concerted activity of these factors is responsible for targeting Arp2/3 specifically to heterochromatic DSBs. We conclude that Arp2/3 is recruited to heterochromatic breaks by Mre11 and HP1a, and mediates relocalization of DSBs to the nuclear periphery in concert with Smc5/6.

Nuclear F-actin is required for relocalization

The presence of Arp2/3 at heterochromatic DSBs suggests that actin polymerizes at these sites to promote relocalization. We targeted to the nucleus a GFP-tagged F-actin chromobody (F-actCB–GFP–NLS) to visualize nuclear actin filaments in vivo without altering actin levels (Extended Data Fig. 3a). Before IR, this marker displays a diffuse nuclear signal, but IR induces the formation of striking filaments surrounding the heterochromatin domain and reaching the nuclear periphery (Fig. 2a, Extended Data Fig. 3b, Supplementary Videos 1, 2). Phalloidin staining of cells with or without the chromobody indicates that these are canonical actin filaments (Extended Data Fig. 3c, d). Consistent with a role for Arp2/3 in filament assembly, filaments are enriched for Arp2/3 (Extended Data Fig. 3e), disrupted by Arp2/3 RNAi or CK666 treatment (Fig. 2b), and characterized by branching at a $70\pm7^{\circ}$ angle 16 (Extended Data Fig. 3f).

Filaments form concurrently with DSB departure from the heterochromatin domain (10–30 min after IR^{5,7}), persist for about 25 min on average, are highly dynamic (suggesting actin remodelling¹⁷), and progressively disappear during relocalization of DSBs to the nuclear periphery (30–60 min after IR⁷) (Fig. 2a–c, Extended Data Figs. 3b, c, g, 4a, Supplementary Videos 2, 3). Most filaments originate from repair foci and the periphery of the heterochromatin domain (Extended Data Fig. 4b). Nearly all filaments (98.6%) remain outside the domain during elongation, suggesting that they tend to polymerize away from the domain. Filament length spans the distance between the heterochromatin domain periphery and the nuclear periphery (Extended Data Fig. 4c). Repair foci decorate actin filaments in fixed samples and travel along the filaments in time-lapse experiments (Fig. 2c, Extended Data Figs. 3d, 4a, Supplementary Video 3). Together, these data suggest that actin filaments have a direct role in relocalization of heterochromatic repair sites to the nuclear periphery.

Triton extraction partially destabilizes actin filaments, resulting in residual chromobody signals that colocalize with phalloidin and repair sites (Extended Data Fig. 3d). Similar colocalization occurs in cells expressing Flag-NLS-tagged wild-type actin (actin(WT)), but not in cells expressing a non-polymerizable R62D mutant (actin(R62D); Fig. 2d, Extended Data Fig. 4e), supporting the presence of F-actin at repair sites. Colocalization between F-actin and DSBs peaks 10-60 min after IR, followed by a marked decline (Fig. 2d). This reduction is likely to result from actin depolymerization, given that expression of a filament-stabilizing S14C mutant induces persistent colocalization (Fig. 2d, Extended Data Fig. 4e). Furthermore, consistent with a role of Arp2/3 in filament formation, colocalization between DSBs and F-actin is affected by RNAi of Arp2/3 or Scar and Wash (Extended Data Fig. 4f). Thus, Arp2/3, Scar and Wash are required to form F-actin at DSBs, with a peak of polymerization during relocalization followed by depolymerization.

We directly tested the role of nuclear F-actin in the relocalization of heterochromatic DSBs by investigating the effect of blocking actin polymerization in the nucleus without altering cytoplasmic F-actin. We expressed actin(WT) or actin(R62D) in the nucleus while blocking nuclear import of endogenous actin by RNAi depletion of the actin-specific importin Ipo9. Wild-type actin expression results in normal

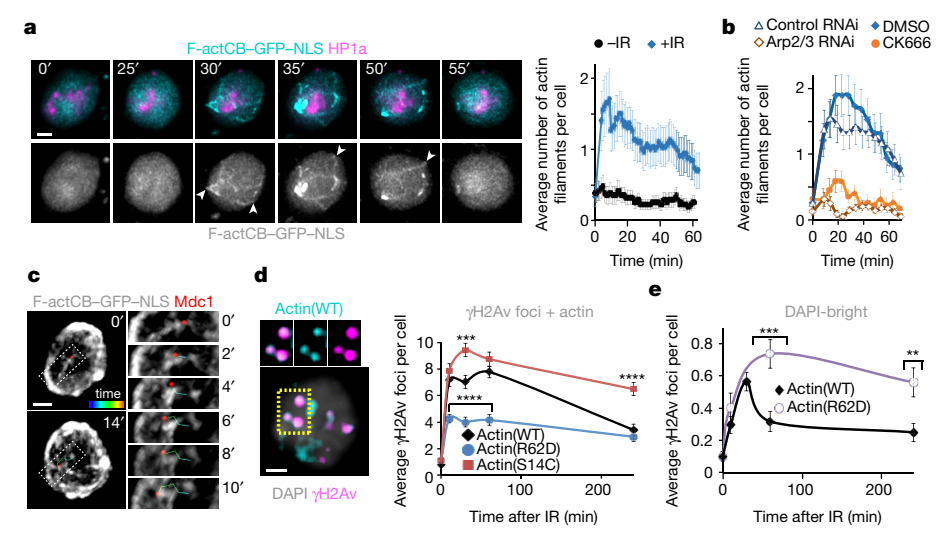


Fig. 2 | Nuclear F-actin is required for relocalization. a, Frames from Supplementary Video 2 and quantification of Kc cells expressing F-actCB-GFP-NLS and mCherry–HP1a (heterochromatin mark⁵) show dynamic filaments in cells treated (+) or not treated (-) with IR. Arrowheads: filaments reaching the nuclear periphery. Time points are after IR (frames and +IR quantification) or from the start of the video (-IR). P < 0.0001, IR-treated versus untreated; $n \ge 22$ cells/experiment. b, As in a but in cells treated with indicated RNAi or CK666. P < 0.0001, control versus Arp2/3 RNAi, DMSO versus CK666, $n \ge 19$ cells per treatment or RNAi. c, Frames from Supplementary Video 3 show a Mdc1 focus moving along actin filaments.

kinetics of focus relocalization, whereas expression of actin(R62D) leads to marked relocalization defects (Fig. 2e, Extended Data Fig. 4g–i). We conclude that nuclear actin polymerizes at repair sites, forms long filaments that reach the nuclear periphery and is required for relocalization of heterochromatic DSBs along the filaments.

Relocalization relies on nuclear myosins

Myosins I and V have been proposed to mediate nuclear dynamics along actin filaments in human cells, including for gene repositioning during transcription 18,19 , chromosome territory reorganization 20 and viral infection 21 . In Drosophila cells, simultaneous RNAi depletion of myosin I (Myo1A and Myo1B) and myosin V (MyoV) results in defective relocalization of heterochromatic DSBs (Fig. 3a, Extended Data Fig. 5a–c). Relocalization is also impaired after nuclear expression of dominant-negative mutants of MyoV (NLS-tagged MyoV $^{\rm headless}$ or MyoV $^{\rm tail}$; Fig. 3a, Extended Data Fig. 5b), consistent with a nuclear function of myosins in relocalization.

Similar relocalization defects occur after RNAi depletion of Unc45 (Fig. 3a, Extended Data Fig. 5a–c), which is required for myosin stability and function. Epistasis analyses reveal that each myosin contributes independently to relocalization, and myosins and Unc45 work in the same pathway as Smc5/6 for relocalization (Fig. 3b, Extended Data Fig. 5d, e). Similar to Arp2/3 RNAi, myosin or Unc45 RNAi does not affect early repair steps (formation of foci containing Mdc1, Atrip, Smc6 or Nse2, or suppression of Rad51 focus formation inside the domain) (Extended Data Figs. 5f, g, 6a), suggesting that myosins act after resection and Smc5/6 recruitment. Myosins, and not other early repair components, co-immunoprecipitate with Smc5/6 in response to IR (Fig. 3c, Extended Data Fig. 6b, c), consistent with a direct interaction between Smc5/6 and myosins for relocalization.

Myosins and Unc45 are enriched at heterochromatic DSBs before relocalization (Fig. 3d, Extended Data Fig. 6e, f), consistent with a specific role in heterochromatin repair. Similarly to Arp2/3, recruitment of myosin to DSBs relies on Mre11 and HP1a, suggesting that the concerted activity of these factors is required to target myosin to heterochromatic DSBs (Fig. 3e). Additionally, recruitment of Unc45, but not of myosins, to DSBs relies on Smc5/6 and SUMO E3-ligases (Fig. 3e). This suggests that recruitment of Unc45 to a pre-assembled

Time points relative to start of focus movement. **d**, Immunofluorescence and quantification of γ H2Av foci colocalizing with Flag–NLS–actin(WT), Flag–NLS–actin(R62D), or Flag–NLS–actin(S14C) at indicated time points. *****P < 0.0001, ***P = 0.0006, $P \ge 0.0001$, ***P = 0.0006, $P \ge 0.0001$, ***P = 0.0001, ***P = 0.0019, **P = 0.00

relocalization machinery (Arp2/3, F-actin and myosins) is the trigger for myosin activation and repair site relocalization downstream of Smc5/6.

The MyoV^{headless} or MyoV^{tail} mutations affect the ability of MyoV to walk along actin filaments, suggesting that this function is required for relocalization. Similarly, treatment of cells with the myosin inhibitor 2,3-butanedione monoxide (BDM) or the MyoV inhibitor MyoVin, which interfere with myosin movement along actin filaments, results in reversible relocalization defects (Extended Data Fig. 6g, h). BDM and MyoVin also affect relocalization in mouse cells (Extended Data Fig. 6i). We conclude that Smc5/6 interacts with nuclear myosins and recruits Unc45 to heterochromatic DSBs, and that this enables relocalization of repair sites through the ability of myosins to walk along actin filaments.

Directed motions of heterochromatic DSBs

Nuclear actin might generate filamentous structures for myosin-mediated trafficking of heterochromatic repair sites, resulting in directed motion²². Alternatively, F-actin and myosin could contribute to relocalization indirectly, for example by local chromatin changes enabling DNA 'looping' from the domain²³ followed by Brownian motion and anchoring at the nuclear periphery. To distinguish Brownian from directed motion, we investigated the biophysical properties of the motion by tracking Mdc1 foci and calculating the mean-square displacement (MSD)²⁴ of focus trajectory in *Drosophila* cells.

MSD curves for heterochromatic foci have a higher plateau than those for euchromatic foci (Fig. 4a, Extended Data Fig. 7a), showing that heterochromatic foci explore a larger space²⁴. This is particularly notable considering that undamaged sites that are embedded in heterochromatin, such as centromeres, display little mobility (Fig. 4a). Heterochromatic foci that reach the nuclear periphery during the 1-h time-lapse (about 20% of all heterochromatic foci) are the most dynamic, while foci that stay inside the heterochromatin domain, move to the domain periphery or persist at the domain periphery show limited mobility (Fig. 4b, Extended Data Fig. 7b). Consistent with a specialized role for the nuclear periphery in heterochromatin repair⁷, euchromatic DSBs rarely move to the nuclear periphery (Extended Data Fig. 7c).

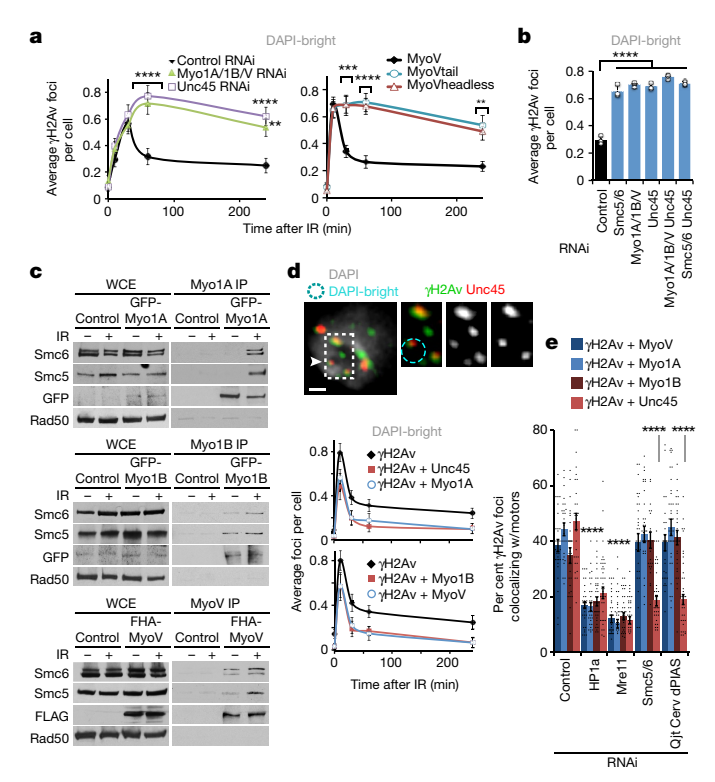


Fig. 3 | Relocalization relies on nuclear myosins. a, Quantification of $\gamma H2 Av$ foci in DAPI-bright heterochromatin in Kc cells fixed at indicated time points after IR, and following indicated RNAi or expression of MyoV forms. ****P < 0.0001, ***P \leq 0.0004, **P \leq 0.0033, $n \geq$ 100 cells per RNAi or cell line, per time point. b, As in a, 1 h after IR. ****P < 0.0001, $n \geq$ 468 cells per RNAi. Control and Smc5/6 as in Fig. 1d. c, Immunoprecipitation of GFP–Myo1A, GFP–Myo1B or FHA–MyoV with Smc5/6 before (-) and after (+) IR and western blotting with indicated antibodies. d, Immunofluorescence and quantification of $\gamma H2 Av$ foci colocalizing with FHA–Myo1A, GFP–Myo1B, MyoV, or Unc45, in DAPI-bright heterochromatin at indicated time points. $n \geq$ 30 cells per time point per experiment. Scale bar, 1 μ m. e, As in d, 10 min after IR, after indicated RNAi. ****P < 0.0001 versus control, n > 24 cells per experiment. Data shown as mean \pm s.e.m. in a, d, e and mean \pm s.d. of at least three independent experiments in b.

While MSD curves reaching a plateau typically describe Brownian motion in a confined space 24 , similar plots also result from averaging MSD curves of asynchronous foci each characterized by different types of motion 22,24 . Indeed, application of a computational method 24 unmasks long-lasting directed motions (LDMs) associated with nearly all heterochromatic foci, mostly occurring between the heterochromatin domain periphery and the nuclear periphery (Fig. 4c, Extended Data Fig. 7d–f). LDMs last 24 ± 2 min (mean \pm s.e.m.), consistent with the average duration of nuclear actin filaments, and are characterized by an average speed of $0.148\pm0.01~\mu m$ min $^{-1}$, consistent with previously described F-actin and myosin-driven chromatin motions 18,25 .

Depletion of Arp2/3 or Unc45 substantially affects the dynamics of heterochromatic foci by reducing the plateaus of MSD curves, the number of foci leaving the domain and LDM frequency (Fig. 4d, e, Extended Data Fig. 7b). Conversely, these depletions do not affect focus dynamics in euchromatin (Fig. 4d, Extended Data Fig. 7g), highlighting a specialized role for Arp2/3 and Unc45 in the directed motion of heterochromatic DSBs. Notably, Arp2/3 (but not Unc45) mediates focus clustering in euchromatin and not in heterochromatin (Extended Data Fig. 7h), revealing that Arp2/3 has distinct functions in the two domains and suggesting that focus clustering does not require extensive dynamics in *Drosophila* cells. The role of Arp2/3 and actin polymerization in focus clustering is conserved in human cells²⁶. We conclude that nuclear actin filaments enable the myosin-dependent directed motion of heterochromatic repair sites to the nuclear periphery.

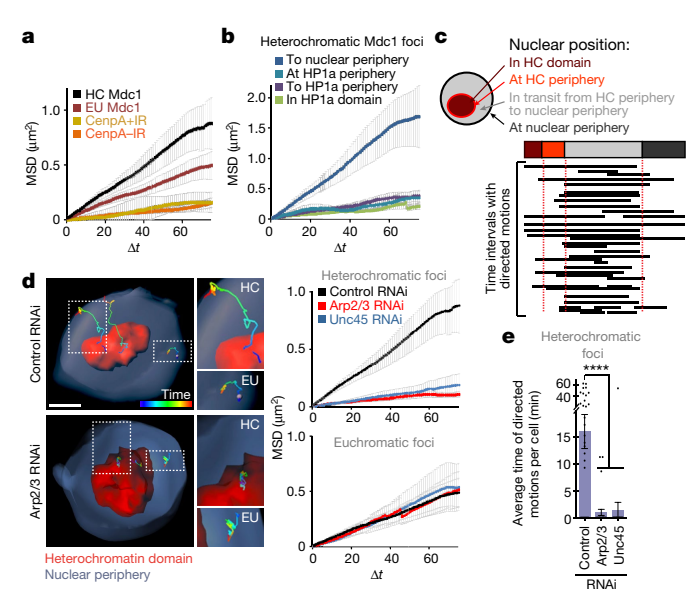


Fig. 4 | Actin nucleators and myosins drive directed motions of heterochromatic DSBs. a, MSD analysis of heterochromatic (HC) or euchromatic (EU) GFP-Mdc1 foci (formed inside or outside the mCherry-HP1a domain, respectively) after IR, or GFP-CenpA foci before (-) and after (+) IR. P < 0.0001 for all comparisons versus heterochromatic Mdc1 foci, $n \ge 19$ tracks per category. Δt , time intervals (intervals were 40 s each). b, MSD analysis of heterochromatic Mdc1 foci from a that remain inside the HP1a domain; move to the domain periphery; remain at the domain periphery; or move to the nuclear periphery. P < 0.0001 for all comparisons versus 'to nuclear periphery category. n = 41 foci. c, LDM analysis of foci that reach nuclear periphery in **b**. Duration and length of LDMs (black lines) are adjusted relative to a 'pseudo-trajectory' defined by the average time that foci spend in each nuclear space. n = 28 foci. **d**, 3D reconstructions in Imaris and MSD analyses of heterochromatic foci that reach the nuclear periphery, or euchromatic foci, after indicated RNAi depletions. Heterochromatic foci: P < 0.0001 versus control, $n \ge 28$ heterochromatic and $n \ge 19$ euchromatic foci per RNAi. e, Quantification of LDM durations of all heterochromatic foci în **d**. ****P < 0.0001 versus control, $n \ge 30$ cells per RNAi. Scale bars, 1 μ m. Data shown as mean \pm s.e.m. P values calculated with extra sum-ofsquares F-test, nonlinear regression for curve fitting for a, b, d and twotailed Mann-Whitney test in e.

Importance for heterochromatin integrity

These results show that nuclear F-actin and myosins drive the relocalization of heterochromatic DSBs, suggesting that these components are important for heterochromatin repair. We directly tested this by determining the biological consequences of inactivating nuclear actin polymerization or myosins. Defective heterochromatin repair results in persistent \(\gamma H2Av \) foci associated with the heterochromatin domain 20 h after IR in fly cells and 16–24 h after IR in mouse ce (that is, at time points when repair is largely completed in euchromatin^{7,27}). Similar defects occur after disruption of homologous pairing (Slmb RNAi) or sister chromatid cohesion (Rad21 and Slmb RNAi) in Drosophila (Extended Data Fig. 8a-c), consistent with the importance of both homologous templates for heterochromatin repair 10. Persistent foci occur after RNAi depletion of Arp2/3, myosins and Unc45, or upon nuclear expression of a non-polymerizable form of actin in fly cells or ARP3 RNAi in mouse cells (Fig. 5a, b, Extended Data Fig. 8d, e). These depletions also impair fly cell survival after IR (Fig. 5c). We conclude that Arp2/3, nuclear F-actin and myosins are critical for the timely progression of heterochromatin repair.

Inactivation of myosins or of actin polymerization triggers the formation of IR-induced heterochromatic micronuclei in fly and mouse cells (Fig. 5d, e, Extended Data Fig. 8f, g), and genome instability in *Drosophila* larval neuroblasts (Fig. 5f, Extended Data Fig. 8h, i). Abnormal karyotypes are likely to be caused by defective

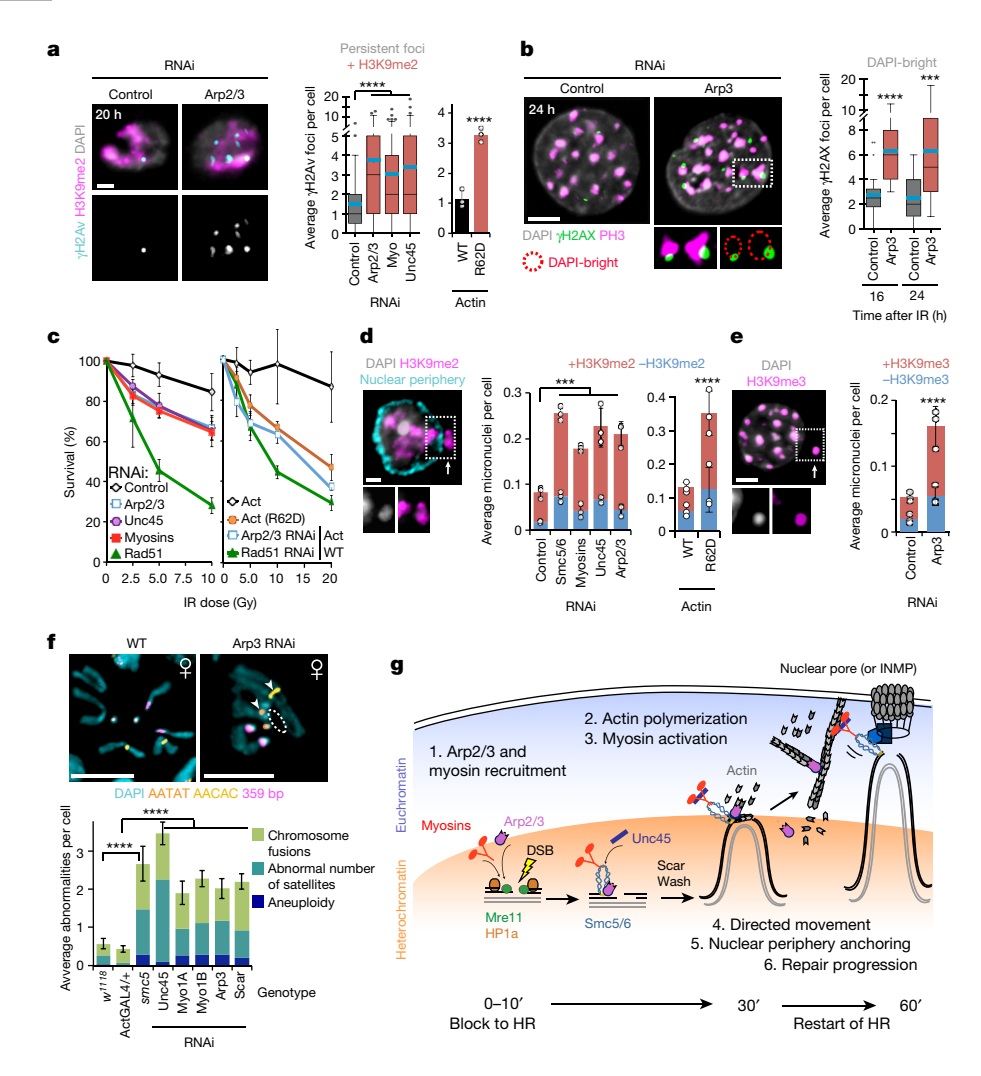


Fig. 5 | Nuclear F-actin and myosins promote heterochromatin **integrity. a**, Immunofluorescence and quantification of γH2Av foci associated with H3K9me2 in Kc cells fixed 20 h after IR, after indicated RNAi or expression of actin forms. ****P < 0.0001, $n \ge 68$ cells per RNAi and n > 220 cells per actin-expressing line. **b**, As in **a** except NIH3T3 G2 cells stained for γ H2AX and PH3. ****P< 0.0001, ***P= 0.0008, $n \ge 20$ cells per RNAi. c, IR sensitivity of Kc cells after indicated RNAi or expression of actin forms. Rad51 RNAi, positive control⁷. P < 0.0001versus control RNAi or wild-type actin (Act), n > 1,324 cells per RNAi; $n \ge 248$ cells per actin-expressing line, per dose. **d**, Immunofluorescence and quantification of micronuclei (arrow) in cells stained for H3K9me2 and nuclear periphery (Nup62) after indicated RNAi or expression of actin forms and IR. *** $P \le 0.0009$, $n \ge 311$ cells per RNAi; ***P < 0.0001, n > 372 cells per actin-expressing line. **e**, As in **d**, except NIH3T3 cells stained for H3K9me3. ****P < 0.0001 versus control; n > 1,450 cells per RNAi. f, Fluorescence in situ hybridization (FISH) and quantification of larval karyotypes stained for indicated satellites show chromosome abnormalities in mutants or RNAi depleted flies versus controls

repair of spontaneous DSBs during larval development. Chromosome rearrangements include aneuploidies, chromosome fusions and changes in the number of satellites (Fig. 5f); most of which involve the heterochromatic fourth and Y chromosomes, or pericentromeric regions, as expected for defective heterochromatin repair (Extended Data Fig. 8i). We conclude that Arp2/3-dependent nuclear actin polymerization and myosins are critical for heterochromatin repair and stability in *Drosophila* cells and tissues, and in mouse cells.

Discussion

Our results revealed a notable role of F-actin and myosins in the directed motion of heterochromatic DSBs to the nuclear periphery. To our

 $(w^{1118} \text{ or ActGAL4/+})$. Arrowheads, chromosome fusions. Dashed circle, arm loss. ****P < 0.0001, n > 36 karyotypes per genotype. Scale bars, 1 μ m in **a**, **d**; 5 μ m in **b**, **e**, **f**. Data shown as mean \pm s.e.m. in **a** (RNAi), **b**, **f** or mean \pm s.d. of at least three independent experiments in **a** (actin), c-e. P values calculated with two-tailed Mann-Whitney test in a, b, d (RNAi); unpaired t-test with Welch's correction in **d** (actin), **e**, **f**; extra sum-of-squares F-test, nonlinear regression for curve-fitting in c. g, Model of heterochromatin relocalization pathway. DSBs are resected inside the heterochromatin domain; Mre11 and HP1a promote the loading of Arp2/3 and nuclear myosins to DSBs; activation of Arp2/3 by Scar and Wash induces formation of actin filaments that reach the nuclear periphery; Unc45 recruitment by Smc5/6 activates nuclear myosins to 'walk' along filaments, thus relocalizing DSBs to nuclear pores or inner nuclear membrane proteins (INMPs)^{5,7,8}; homologous recombination continues while filaments disassemble. Relocalization prevents ectopic recombination by isolating damaged sites and their homologous templates (grey lines) from undamaged heterochromatic repeats before strand invasion.

knowledge, we have shown for the first time by live imaging the formation, structure and remodelling of IR-induced nuclear actin filaments and the movement of repair sites along them. Filaments form at repair sites, reach the nuclear periphery and disassemble after relocalization. We have also identified a specialized network of proteins that coordinates heterochromatin dynamics and nuclear actin filament formation in concert with Smc5/6, including Arp2/3; the Arp2/3 activators Scar and Wash; the nuclear myosins Myo1A, Myo1B and MyoV; and the myosin activator Unc45. Arp2/3 and myosins are targeted to heterochromatic DSBs by Mre11 and the heterochromatin component HP1a. Recruitment of Unc45 also requires Smc5/6 and SUMO E3-ligases, suggesting that Unc45 is a trigger for the myosin-dependent movement

of heterochromatic DSBs along actin filaments downstream of Smc5/6. This pathway appears to be conserved in mouse cells, and its deregulation results in heterochromatin repair defects and instability. These results support a model in which DSBs in heterochromatin induce the formation of nuclear actin filaments that connect repair sites to the nuclear periphery. Smc5/6-associated myosins travelling along these 'highways for repair' enable the directed movement of repair sites to the nuclear periphery for safe progression of homologous recombination repair (Fig. 5g).

Nuclear repositioning of repair sites has been observed in different contexts^{1,2}, including DSBs in rDNA^{28,29}, damaged telomeric and subtelomeric sequences^{30–35}, collapsed replication forks^{36,37}, persistent DSBs^{36,38–40}, and homology search^{41,42}. Cytoplasmic microtubules contribute to some of these dynamics via the trans-nuclear membrane LINC complex^{35,40}. However, the nuclear structures responsible for those movements have remained largely unknown, and Brownian motions are thought to account for most of these dynamics²³.

Directed motions might be especially needed to leave the heterochromatin domain, given the compact nature of this domain and its potential resistance to releasing repair sites. Accordingly, Arp2/3 and myosins affect directed motions in heterochromatin and not in euchromatin. Notably, Arp2/3-dependent nuclear actin filaments form loose branches, distinct from the dense cytoplasmic network that mediates cell movement. This is likely to reflect specialized Arp2/3 regulation and F-actin remodelling¹⁷ in the nucleus for the directed motion of repair sites. These studies identify nuclear F-actin and myosins as critical components for heterochromatin repair and genome stability in multicellular eukaryotes.

Online content

Any Methods, including any statements of data availability and Nature Research reporting summaries, along with any additional references and Source Data files, are available in the online version of the paper at https://doi.org/10.1038/s41586-018-0242-8.

Received: 15 June 2017; Accepted: 18 May 2018; Published online 20 June 2018.

- Amaral, N., Ryu, T., Li, X. & Chiolo, I. Nuclear dynamics of heterochromatin repair. Trends Genet. 33, 86–100 (2017).
- Caridi, P. C., Delabaere, L., Zapotoczny, G. & Chiolo, I. And yet, it moves: nuclear and chromatin dynamics of a heterochromatic double-strand break. *Phil. Trans.* R. Soc. Lond. B 372, 20160291 (2017).
- Ho, J. W. et al. Comparative analysis of metazoan chromatin organization. Nature 512, 449–452 (2014).
- Hoskins, R. A. et al. The Release 6 reference sequence of the Drosophila melanogaster genome. Genome Res. 25, 445–458 (2015).
- Chiolo, İ. et al. Double-strand breaks in heterochromatin move outside of a dynamic HP1a domain to complete recombinational repair. Cell 144, 732–744 (2011).
- Čhiolo, I., Tang, J., Georgescu, W. & Costes, S. V. Nuclear dynamics of radiationinduced foci in euchromatin and heterochromatin. *Mutat. Res.* 750, 56–66 (2013).
- Ryu, T. et al. Heterochromatic breaks move to the nuclear periphery to continue recombinational repair. Nat. Cell Biol. 17, 1401–1411 (2015).
- Ryu, T., Bonner, M. R. & Chiolo, I. Cervantes and Quijote protect heterochromatin from aberrant recombination and lead the way to the nuclear periphery. Nucleus 7, 485–497 (2016).
- Li, Q. et al. The three-dimensional genome organization of *Drosophila melanogaster* through data integration. Genome Biol. 18, 145 (2017).
- Janssen, A. et al. A single double-strand break system reveals repair dynamics and mechanisms in heterochromatin and euchromatin. Genes Dev. 30, 1645–1657 (2016).
- Jakob, B. et al. DNÁ double-strand breaks in heterochromatin elicit fast repair protein recruitment, histone H2AX phosphorylation and relocation to euchromatin. *Nucleic Acids Res.* 39, 6489–6499 (2011).
- Tsouroula, K. et al. Temporal and spatial uncoupling of DNA double strand break repair pathways within mammalian heterochromatin. Mol. Cell 63, 293–305 (2016).
- Andrin, C. et al. A requirement for polymerized actin in DNA double-strand break repair. Nucleus 3, 384–395 (2012).
- Belin, B. J., Lee, T. & Mullins, R. D. DNA damage induces nuclear actin filament assembly by Formin -2 and Spire-1/2 that promotes efficient DNA repair. eLife 4, e07735 (2015).
- Sun, M. H. et al. DNA double-strand breaks induce the nuclear actin filaments formation in cumulus enclosed oocytes but not in denuded oocytes. *PLoS ONE* 12, e0170308 (2017).

- Mullins, R. D., Heuser, J. A. & Pollard, T. D. The interaction of Arp2/3 complex with actin: nucleation, high affinity pointed end capping, and formation of branching networks of filaments. *Proc. Natl Acad. Sci. USA* 95, 6181–6186 (1998).
- 17. Goley, E. D. & Welch, M. D. The ARP2/3 complex: an actin nucleator comes of age. *Nat. Rev. Mol. Cell Biol.* **7**, 713–726 (2006).
- 18. Chuang, C.-H. et al. Long-range directional movement of an interphase chromosome site. *Curr. Biol.* **16**, 825–831 (2006).
- Dundr, M. et al. Actin-dependent intranuclear repositioning of an active gene locus in vivo. J. Cell Biol. 179, 1095–1103 (2007).
- Mehta, I. S., Amira, M., Harvey, A. J. & Bridger, J. M. Rapid chromosome territory relocation by nuclear motor activity in response to serum removal in primary human fibroblasts. Genome Biol. 11, R5 (2010).
- Roberts, K. L. & Baines, J. D. Actin in herpesvirus infection. Viruses 3, 336–346 (2011).
- 22. Hatakeyama, H., Nakahata, Y., Yarimizu, H. & Kanzaki, M. Live-cell single-molecule labeling and analysis of myosin motors with quantum dots. *Mol. Biol. Cell* 28, 173–181 (2017).
- Amitai, A., Seeber, A., Gasser, S. M. & Holcman, D. Visualization of chromatin decompaction and break site extrusion as predicted by statistical polymer modeling of single-locus trajectories. *Cell Reports* 18, 1200–1214 (2017).
- Caridi, C. P. et al. Quantitative methods to investigate the 4D dynamics of heterochromatic repair sites in *Drosophila* cells. *Methods Enzymol.* 601, 359–389 (2018).
- Li, H., Guo, F., Rubinstein, B. & Li, R. Actin-driven chromosomal motility leads to symmetry breaking in mammalian meiotic oocytes. *Nat. Cell Biol.* 10, 1301–1308 (2008).
- Schrank, B. R. et al. Nuclear ARP2/3 drives DNA break clustering for homologydirected repair. Nature https://doi.org/10.1038/s41586-018-0237-5 (2018).
- Goodarzi, A. A. et al. ATM signaling facilitates repair of DNA double-strand breaks associated with heterochromatin. Mol. Cell 31, 167–177 (2008).
- Torres-Rosell, J. et al. The Smc5–Smc6 complex and SUMO modification of Rad52 regulates recombinational repair at the ribosomal gene locus. Nat. Cell Biol. 9, 923–931 (2007).
- van Sluis, M. & McStay, B. A localized nucleolar DNA damage response facilitates recruitment of the homology-directed repair machinery independent of cell cycle stage. Genes Dev. 29, 1151–1163 (2015).
- Therizols, P. et al. Telomere tethering at the nuclear periphery is essential for efficient DNA double strand break repair in subtelomeric region. *J. Cell Biol.* 172, 189–199 (2006).
- 31. Khadaroo, B. et al. The DNA damage response at eroded telomeres and tethering to the nuclear pore complex. *Nat. Cell Biol.* **11**, 980–987
- 32. Čho, N. W., Dilley, R. L., Lampson, M. A. & Greenberg, R. A. Interchromosomal homology searches drive directional ALT telomere movement and synapsis. *Cell* **159**, 108–121 (2014).
- Chung, D. K. et al. Perinuclear tethers license telomeric DSBs for a broad kinesin- and NPC-dependent DNA repair process. *Nat. Commun.* 6, 7742 (2015).
- Churikov, D. et al. SUMO-dependent relocalization of eroded telomeres to nuclear pore complexes controls telomere recombination. *Cell Reports* 15, 1242–1253 (2016).
- Lottersberger, F., Kárssemeijer, R. A., Dimitrova, N. & de Lange, T. 53BP1 and the LINC complex promote microtubule-dependent DSB mobility and DNA repair. Cell 163, 880–893 (2015).
- Nagai, S. et al. Functional targeting of DNA damage to a nuclear poreassociated SUMO-dependent ubiquitin ligase. Science 322, 597–602 (2008).
- Su, X. A., Dion, V., Gasser, S. M. & Freudenreich, C. H. Regulation of recombination at yeast nuclear pores controls repair and triplet repeat stability. *Genes Dev.* 29, 1006–1017 (2015).
- Kalocsay, M., Hiller, N. J. & Jentsch, S. Chromosome-wide Rad51 spreading and SUMO-H2A.Z-dependent chromosome fixation in response to a persistent DNA double-strand break. Mol. Cell 33, 335–343 (2009).
- Oza, P., Jaspersen, S. L., Miele, A., Dekker, J. & Peterson, C. L. Mechanisms that regulate localization of a DNA double-strand break to the nuclear periphery. *Genes Dev.* 23, 912–927 (2009).
- Swartz, R. K., Rodriguez, E. C. & King, M. C. A role for nuclear envelope-bridging complexes in homology-directed repair. Mol. Biol. Cell 25, 2461–2471 (2014).
- Dion, V., Kalck, V., Horigome, C., Towbin, B. D. & Gasser, S. M. Increased mobility of double-strand breaks requires Mec1, Rad9 and the homologous recombination machinery. *Nat. Cell Biol.* 14, 502–509 (2012).
- Miné-Hattab, J. & Rothstein, R. Increased chromosome mobility facilitates homology search during recombination. *Nat. Cell Biol.* 14, 510–517 (2012).

Acknowledgements Work supported by USC Gold Family and Research Enhancement Fellowships to T.R., and R01GM117376, Mallinckrodt Foundation Award, and NSF Career 1751197 to I.C. We thank S. Keagy, O. Aparicio and the Chiolo Laboratory for comments; O. Aparicio, M. Michael and V. Longo for reagents and cells; B. Mellone, G. Posern and S. Celniker for plasmids; L. Cooley, A. Eprussi, H. Ohkura, M. Gatti, S. Bernstein, G. Karpen, J. Kadonaga, S. Elgin, S. Parkhurst and DSHB for antibodies; F. Cuturale, C. Artesano, S. Fraser and the Translation Imaging Center for help with imaging and analyses; H. Hopp, B. Spatola, P. Palagani and A. Holcom for experimental help; and the BDSC (P400D018537), VDRC, and DGRC (P400D010949) for flies and plasmids. We apologize to our colleagues whose work could not be cited owing to space limitations.



Author contributions C.P.C. and C.D. performed most experiments; T.R. performed experiments for Figs. 1e, 3a, c, 5c–e and Extended Data Figs. 1f, g, 2i, 4i, 5d, 6c, h, 8c; G.Z. for Figs. 1b, 3a, 5b, e and Extended Data Figs. 1k, 2f, 6i; L.D. for Extended Data Figs. 3e, 8h and complementary studies; X.L. for Fig. 5f and Extended Data Fig 8h; V.Y.K for Fig. 3a and Extended Data Figs. 1g, 6b, h, 8a–c, f; N.A. for Fig. 2a, d; E.L. for Fig. 5c; and A.R.R. for Extended Data Fig. 8h. I.C. conceived and supervised the project, contributed to experiments and wrote the manuscript.

Competing interests The authors declare no competing interests.

Additional information

Extended data is available for this paper at https://doi.org/10.1038/s41586-018-0242-8.

Supplementary information is available for this paper at https://doi.org/10.1038/s41586-018-0242-8.

Reprints and permissions information is available at http://www.nature.com/reprints.

Correspondence and requests for materials should be addressed to I.C. **Publisher's note:** Springer Nature remains neutral with regard to jurisdictional claims in published maps and institutional affiliations.

METHODS

Cell culture and generation of stable cell lines. Kc167 (Kc) cells were used for most experiments and were maintained as logarithmically growing cultures in Schneider's medium (Sigma) + FBS (Gemini). Kc cells were authenticated by the Drosophila Genomic Resource Center (DGRC) and no mycoplasma contamination was detected Stable lines were obtained by cotransfecting the plasmid of interest with pCoHygro (Invitrogen) or pCoPuro (Addgene) and selecting in the presence of 100 μ g/ml hygromycin B (Invitrogen) or 2 mg/ml puromycin (Enzo Life Sciences). Transfection was performed with DOTAP (Roche) or Cellfectin (Life Technologies), according to the manufacturers' protocols. Mouse NIH3T3 cells (gift from V. Longo) were maintained at 30–80% confluency in DMEM (Corning) + 10% CBS (Denver Serum Company).

IR treatments. Cell cultures were exposed to IR using a 160 kV X-ray source (X-RAD iR-160, Precision X-Ray). For *Drosophila* cells, we mostly use a range of Gy at which the damage response increases linearly with dose (1.7–20 Gy), and corresponds to nearly sublethal doses for controls? A dose of 5 Gy was used for most experiments, unless otherwise indicated. Treatments with this dose do not affect nuclear–cytoplasmic transport, which was evaluated by measuring the ratio between nuclear and cytoplasmic GFP-tagged Myo1A, Myo1B, MyoV, Arp2, Arp3 and Unc45. The estimated number of DSBs induced by 5 Gy in *Drosophila* cells is ~7.5 DSBs in G1 and ~14 DSBs in G2⁷. In kinetic analyses of fixed cells, time 0 corresponds to cells fixed without exposure to IR. In time-lapse experiments, time 0 corresponds to cells imaged 5–10 min before IR treatment unless otherwise specified. Mouse cells were exposed to 1 Gy, similar to previous studies^{27,44,45}.

Plasmids. pCopia-GFP-Mdc1, pCopia-mCherry-HP1a, pCopia-GFP-Smc5, pCopia-GFP-Nse2, pCopia-GFP-Atrip, and pCopia-GFP-CenpA plasmids were previously described^{5,7,46}. All other GFP- and FHA (3×Flag-3×HA)-tagged proteins were generated by insertion of PCR-amplified coding regions of cDNAs from DGRC or other sources. Clone numbers from DGRC were: Arp2 (LD18955), Arp3 (LD35711), Myo1A (SD01662), Myo1B (FI19407) and Unc45 (SD10334). Detailed information is available on the DGRC website (http://dgrc.cgb.indiana. edu). Arp2/3 has previously been identified as a major actin-nucleating factor in *Drosophila*⁴⁷. Functions of Unc45 in myosin regulation have been described⁴⁸. Wild-type actin and the two mutant constructs actin(S14C) and actin(R62D) were PCR amplified from pEF-Flag-NLS-βActin, pEF-Flag-NLS-βActin(S14C) or pEF-Flag-NLS-βActin(R62D)⁴⁹ (gift from G. Posern). MyoV was generated by PCR amplification of clone FI23904 (ref. 2014422, gift from S. Celniker). The actin chromobody was generated by PCR amplification of actin-chromobody-TagGFP2-NLS plasmid⁵⁰. MyoV^{headless} and MyoV^{tail} mutants were generated by PCR amplifications of truncated versions of MyoV, according to ref. 51. All PCR products were cloned into pCopia-LAP-EGFP vectors⁵², or pCopia-3×Flag-StrepII-3×HA vectors⁵. pCopia-mCherry-Mdc1 was generated by swapping the Mdc1 gene from pCopia-GFP-Mdc1 into a pCopia-mCherry vector⁵.

dsRNA synthesis and sequences. siRNAs for RNAi depletions in Drosophila cultured cells were prepared with the MEGAscript T7 Kit (Applied Biosystems). dsRNA derived from the brown (bw) gene was used as control in all experiments. Amplicons and RNAi conditions for bw, Smc5, Smc6 and Rad51 were as previously described⁵. Amplicons used for all other dsRNAs were: DRSC25363/DRSC34284 for Myo1A, DRSC27633 for Myo1B, DRSC07603/ DRSC40837 for MyoV, DRSC15449 for Unc45, DRSC31428/DRSC19332 for Arp2, DRSC29666/DRSC31430 for Arp3, DRSC03426/BKN22532 for Scar, DRSC37426/DRSC06302 for Wash, DRSC26170/DRSC15032 for Wasp, DRSC03519/DRSC24127 for Dia, DRSC03619/DRSC24744/DRSC40746 for Spire, DRSC40055 for Ipo9, DRSC17056/DRSC32610 for Slmb and DRSC20839/DRSC38781 for Rad21. Sequences can be found on the DRSC website (http://flyrnai.org). dsRNA for Whamy RNAi was prepared with the oligonucleotides: 5'GAATTAATACGACTCACTATAGGGAGACGGAATAC GGATTATCCGCC and 5' GAATTAATACGACTCACTATAGGGAGAGATGCAG AAATCACAGCCCAA. Wash, Scar, Whamy and Wasp are the previously $described\ Wiskott-Aldrich\ Syndrome\ protein\ family\ in\ flies^{53}.\ When\ more\ than$ one amplicon is indicated, we combined equal amounts of each dsRNA for better efficiency of protein depletion. For mouse cells, RNAi experiments were conducted using SMARTpool ON-TARGETplus ARP3 siRNA (Dharmacon) and a corresponding non-targeting RNAi control.

RNAi depletion. For *Drosophila* cells, dsRNAs were transfected with DOTAP (Roche) following the manufacturer's instructions and depletion was done for 5 days before performing experiments, except for Slmb and Rad21 RNAi, for which this was done for 4 days. We did not detect significant effects of the RNAi depletions shown in this paper on cell cycle progression by FACS, or on the heterochromatin domain by live imaging of GFP–HP1a-expressing cells. Additionally, RNAi depletion of Arp2/3, myosins or Unc45 did not affect nuclear pore structure by Nup62 immunofluorescence staining. Notably, studies in flies have shown that loss of Wash affects association of HP1a with heterochromatic sequences⁵⁴. However,

depletion of Wash in Kc cells did not affect the mCherry–HP1a signal, indicating that the heterochromatin domain was still largely intact in the RNAi conditions used in Fig. 1c and Extended Data Figs. 1b, l, 4f. This supports a model in which Wash works downstream of HP1a in the relocalization of heterochromatic DSBs. We also note that all kinetics resulting from RNAi depletion must be compared to cells treated with control dsRNAs, as the $\gamma H2Av$ peak shifts from 10 min after IR in non-RNAi experiments (for example, Fig. 1f) to 30 min after IR in RNAi controls (for example, Fig. 1a). RNAi depletion efficiencies for Smc5/6, Nse2/Cerv, Nse2/Qjt, dPIAS, HP1a and Rad51 have previously been validated $^{5.7,8}$. Mouse cells were transfected using Lipofectamine RNAiMAX reagent (Thermo Fisher Scientific) for 2 days before the experiments.

Quantitative PCR. qPCR analysis of RNAi depletions in Drosophila cultured cells was performed as described⁷. Changes in transcript levels were normalized to Ebony, CG12493 or Actin5c mRNA. Primer sequences were: CGCACGGAAATTATCAAGGT and GTCTGCTCGTCATCCTCCTC for Ipo9; ATCATTCACTCCAATTTTACT and AGTAATCTGGTTATTAGTGGAA for Whamy, GGCTGAAGAAGAGCAACCAC and TCACCTTGCGCAACT GACCAG for Spire; GCGAGTTGTTCCCCAAGATA and GGAGACAATCTT GCCGTCAT for Slmb. For qPCR analysis of RNAi depletions in flies, total RNA was isolated from 5-10 larvae by Trizol extraction and treated with DNase I to remove genomic DNA. RNA was used to generate single-stranded cDNA using oligo dT priming and Superscript Reverse Transcriptase III (Invitrogen). Primer sequences were: CTTAACGAAGACCTGAATGAGGC and CGA CAGTGTCTCCTGTTCCAG for Lamin; GAATGCCCCACATTTGTTCGC and ACCGGAAATTAGGATGCAGGT for Myo1A; AGAGCGAAGAAGCCTT CATCG and GCTTGTAGGGATTCACGGAGAT for Myo1B. Transcripts were quantified with iQ SYBR Green Supermix (Bio-Rad) according to the manufacturer's instruction. Changes in transcript levels were normalized to Lamin mRNA. In both cultured cells and flies, each qPCR was repeated at least three times, and graphs show the average level of depletion relative to control RNAi. qPCR analysis of Arp3 RNAi depletion in mouse cells was done using two independent primer sets for both Arp3 and the control mRNA Gapdh, and the qPCR was repeated twice for each set. Averaged values were normalized for each GAPDH qPCR and averaged between each other. The primer sequences used for this analysis were: AAGAATGAAGCGGACAGGAC and AGTTGGTGATTCCTAGCGTG (set 1) AATCACCAACTTCCCCATCC and AAACCTTCTCACACAGCCTC (set 2) for Arp3; CTTTGTCAAGCTCATTTCCTGG and TCTTGCTCAGTGTCCTTGC (set 1) and GCCTTCCGTGTTCCTACC and CCTCAGTGTAGCCCAAGATG (set 2) for GAPDH.

Immunofluorescence and quantification in fixed samples. Chromosome preparation and FISH protocols used in Fig. 5f and Extended Data Fig. 8b, i were as previously described^{7,9,55}. AACAC, AATAT and 359-bp probes were designed as previously described⁵⁵ and were purchased from Integrated DNA Technologies. Probe sequences are: 5'-6-FAM-(AACAC)₇, 5'-Cy3-TTTTCCAAATTTCGGTCATCAAATAATCAT, and 5'-Cy5-(AATAT)6, respectively. Immunofluorescence without triton extraction was used for most experiments as previously described⁵. Immunofluorescence staining of myosins, Unc45, Arp2/3 complex subunits, Flag-NLS-actin (actin(WT), actin(R62D) and actin(S14C) in Fig. 2d and Extended Data Fig. 4d, e), and F-actCB-GFP-NLS in Extended Data Fig. 3d, was preceded by a triton extraction step as previously described⁷. Notably, these Triton extraction treatments partially destabilize actin filaments 56-58. Detection of nuclear actin filaments with phalloidin in Extended Data Fig. 3c was done by fixing cells for 10 min at 37 °C in pre-warmed, freshly made, fixation buffer (4% PFA, 0.5% Triton-X100, 2 mM ATP, 0.004% NaAz, 1 mM Na3VO4, 1 mM NaF, 1 mM PMSF, protease inhibitor tablets (Roche), phalloidin 1:500; modified from published protocols^{59,60}). Imaging and image processing for fixed cells and tissues has previously been described^{5,7}. Quantification of repair foci relative to DAPI-bright in *Drosophila* cells was done as previously described^{5,7}. Quantification of repair foci relative to H3K9me2 in Drosophila cells was done as previously described⁷. Quantification of repair foci relative to DAPI-bright in mouse cells was done on volume reconstructions and only cells in G2 were used; detection of G2 cells was based on PH3 staining as previously described⁴⁴. For quantification of actin filaments in Extended Data Fig. 3c, filaments were detected with phalloidin (1:500 Alexa Fluor 488, Invitrogen, A12379), imaged with 0.2-µm intervals between the z stacks, and images were deconvolved 20 times with a conservative protocol. Filaments inside the nuclei were identified using DAPI staining as a reference. Figures shown are maximum intensity projections of a few z stacks across the heterochromatin domain(s) (Figs. 1a, b, 5a, b; Extended Data Fig. 1a), individual z stacks or maximum intensity projections of 2–3 z stacks (Figs. 1f, 2d, 3d, 5f, Extended Data Figs. 1d, 2g, 3c, d, e, 4b, d, e, 6e, 8i), maximum intensity projections of all z stacks across the nucleus (Fig. 5d, e, Extended Data Fig. 8b), or volume reconstructions (Figs. 2a, 4d, Extended Data Figs. 2a, c, 3b, f, 4a, 5f, g, 7a).

Western blotting. Protein extraction and western blotting to validate RNAi depletions were conducted as previously described⁷.

Immunoprecipitation. Immunoprecipitation experiments were performed as previously described 7 . For Myo1A immunoprecipitation, 3×10^8 Kc cells expressing GFP–Myo1A, or Kc cells as a control, were pelleted and snap-frozen before and 25 min after exposure to 20 Gy IR. Pellets were incubated in lysis buffer A (50 mM Hepes, 10 mM KCl, 2 mM MgCl2, 20% glycerol, 1 mM PMSF, 20 mM NaF, 20 mM glycerol-2-phosphate, 1 mM benzamidine, 0.5% NP-40, 25 mM NEM, 150 mM NaOAc, 250 mM NaCl, and protease inhibitors (Complete, Roche)), and digested with 1 μ l benzonase (EMD Millipore) at 4 $^{\circ}$ C for 30 min. Pellets were centrifuged and soluble lysates collected. Pellets were resuspended in buffer A and extracted with 300 mM sodium acetate for 1 h at 4 $^{\circ}$ C. Next, the supernatant was pooled with the soluble lysate. Samples were incubated for 3 h at 4 $^{\circ}$ C with protein G-coupled sepharose beads and 5 μ l goat anti-GFP antibody. Beads were washed 5 times with wash buffer A (50 mM Hepes, 10 mM KCl, 2 mM MgCl₂, 20% glycerol, 0.5% NP-40, 350 mM NaCl, 150 mM NaOAc, and 25 mM NEM) and heated in loading buffer for 3 min at 95 $^{\circ}$ C for SDS–PAGE.

For Myo1B, Arp3 and Nse2 immunoprecipitation, 3×10^8 Kc cells expressing GFP–Myo1B, GFP–Arp3 or FHA–Nse2 were pelleted and snap-frozen before and 25 min after exposure to 20 Gy IR. Pellets were incubated with lysis buffer C (50 mM Hepes/KOH pH 7.5, 140 mM NaCl, 1 mM EDTA, 1% Triton X-100, 0.05% Na-deoxycholate, 25 mM NEM) for 30 min at 4°C. Lysates were pelleted and the supernatant was incubated with 1 μ l of benzonase (EMD Millipore) for 30 min at 4°C. Next, supernatants were incubated with Flag–M2 agarose beads (Sigma) for Nse2 or protein G-coupled sepharose beads and 5 μ l goat anti-GFP antibody for Myo1B for 4 h at 4°C. Samples were washed once with lysis buffer C and four times with wash buffer B (100 mM Tris pH 8.0, 250 mM NaCl, 1 mM EDTA, 0.5% NP-40, 0.1% Na- deoxycholate), before heating them in loading buffer for 3 min at 95°C for SDS–PAGE. As a control for Myo1B immunoprecipitation, GFP–Myo1B cells were incubated with sepharose beads without antibodies. Kc cells were used as control for Nse2 and Arp3 immunoprecipitation.

For MyoV immunoprecipitation, 3×10^8 Kc cells expressing FHA–MyoV, or cells without the FHA–MyoV plasmid as a control, were used. Cells were pelleted and snap-frozen before and 25 min after exposure to 20 Gy IR. Pellets were incubated in lysis buffer B (50 mM Tris, 150 mM NaCl, 2 mM EDTA, 10% glycerol, 0.2% Nonidet P-40, protease inhibitors (Complete, Roche), 1 mM PMSF, and 25 mM NEM) for 30 min at 4 °C. Lysates were centrifuged and the supernatant was incubated with Flag–M2 agarose beads (Sigma). Samples were incubated with beads at 4 °C for 5 h. Beads were washed 5 times with lysis buffer B and heated in loading buffer for 3 min at 95 °C for SDS–PAGE.

Cytoplasmic and nuclear actin fractionation. Protocols were adapted from published methods⁶¹. All steps were carried out in ice or in a cold room. First, 10⁷ cells were collected, washed once with ice-cold phosphate-buffered saline (PBS), and pelleted by centrifugation at 800g for 10 min. Cell pellets were placed at -80 °C for 1 h. Then, pellets were resuspended gently on ice in 200 µl buffer P1 (HEPES 10 mM, EGTA 0.1mM, DTT 1 mM, complete protease inhibitors (Roche)). After addition of Triton X-100 (final concentration 0.5%), samples were vortexed on the highest setting for 10 s followed by centrifugation at 4°C, 10,000g for 10 min. One hundred and fifty microlitres of supernatant was collected for the cytoplasmic fraction. The remaining supernatant was removed and discarded. The cytoplasmic fraction was centrifuged at 16,000g, transferred to a new tube, and placed at −80 °C. The nuclear pellet was gently resuspended in 1 ml buffer P1 followed by centrifugation at 4°C, 10,000g for 10 min. The supernatant of the nuclear fraction was discarded and nuclear pellet lysed in $50\,\mu l$ buffer P2 (20 mM HEPES, 25%glycerol, 400 mM NaCl, 1 mM EGTA, 1 mM DTT, complete protease inhibitors (Roche)) by vortexing for 90 min at 4°C. Nuclear extract was clarified by centrifugation at 20,000g for 10 min. The samples were stored at -80 °C until SDS-PAGE and western blotting were performed. Twenty-five micrograms of protein extract $% \left(1\right) =\left(1\right) \left((nuclear or cytoplasmic) was loaded onto an SDS-PAGE gel, per lane.

Chemical treatments. Myosin and actin polymerization inhibitors were added to the cultures before IR treatments. In *Drosophila* cells, treatment conditions were: 2 mM and 10 mM BDM 62 (Sigma) for 5 min; 200 and 400 μ M MyoVin-1 63 (Calbiochem) for 2 h; 100 μ M and 400 μ M CK666 64 (Sigma) for 60 min; 4 μ M and 8 μ M latrunculin B 65 (Enzo Life Sciences) for 20 min. Stocks of MyoVin-1 (100 mM), CK666 (100 mg/ml) and latrunculin B (10 mM) were prepared in DMSO and those of BDM were diluted in water. For mouse cells, treatment conditions were: 7.5 mM BDM for 20 min; 200 μ M MyoVin-1 for 60 min; 400 μ M CK666 for 60 min; 8 μ M latrunculin B for 20 min. All stocks were prepared in DMSO. For controls, DMSO or water was added to the medium to yield final concentrations equivalent to samples treated with chemicals. For the 'release' time points shown in Extended Data Figs. 1f, g, 6h, Kc cells were washed 3 times after incubation with each chemical, and incubated at 27 °C for 1 h before IR. Cells were fixed 60 min after IR. Notably, the doses of LatB treatments used affect nuclear actin polymerization in addition to cytoplasmic actin 65 .

Cell imaging and processing in time-lapse experiments. For MSD analyses, cells stably expressing GFP-Mdc1 and mCherry-HP1a were imaged before and after

IR as described²⁴. In brief, imaging after IR was done every 40 s for 60 min starting from 3–5 min after IR^{7,24}. Ten z stacks at 0.8 μ m distance were imaged for 0.005 ms for GFP, and 0.015 ms for mCherry. The Coolsnap HQ2 camera was set at 2 \times 2 binning to maximize the light collected while minimizing light exposure and cell phototoxicity. Accordingly, these imaging conditions did not induce DSB formation or affect cell division (Extended Data Fig. 7a). All videos were corrected to compensate for modest photobleaching effects using softWoRx (Applied Precision/ GE Healthcare). For each nucleus, 6-12 of the most stationary and spatially distant foci were tracked with Imaris (Bitplane) and used as a reference for registering the nucleus as previously described²⁴. Foci were tracked in 3D using a semiautomated method and manually corrected to ensure optimal connections between time points²⁴. For live imaging experiments, IR dose was lowered from 5 Gy to 1.7 Gy to reduce the average number of Mdc1 foci per nucleus and the frequencies of ambiguous tracks. Focus positional data were extracted in Excel and analysed in Matlab (MathWorks) using a customized script²⁴. MSDs were calculated as previously described²⁴. Positional data were also analysed using a customized script in R Studio to detect LDMs²⁴. In brief, the script derives MSD curves for time intervals $\Delta t > 10$ and increasing starting time points for each trajectory, and identifies time intervals characterized by MSD graphs with increasing slopes^{22,59}. LDMs shown in Fig. 4c and Extended Data Fig. 7d correspond to the largest contiguous time interval containing MSDs of increasing slope for each focus. The ability of the script to correctly detect directed motions was confirmed by independent MSD analysis of the positional data within the time intervals of the LDMs, as shown in Extended Data Fig. 7e. For live imaging of nuclear actin filaments, a stable cell line expressing F-actCB-GFP-NLS was exposed to 5 Gy IR. The same field of cells was imaged before and every 5 min after IR for 60 min. Ten z stacks at 0.8 µm distance were imaged, starting 3-12 min after IR. 3D volume reconstructions and movie generation were done in Imaris (Bitplane). Quantification of filament length and angles of actin branches was done using the Measurement Tool in Imaris.

IR sensitivity assay. The IR sensitivity assay for RNAi depletion experiments (Fig. 5c, left) was done as previously described 7 . Quantification of IR sensitivity for cells expressing actin(WT) or actin(R62D) (Fig. 5c, right) was done using a trypan blue exclusion test for cell viability 66 .

Micronucleus assays. The micronucleus assay in Kc cells was done as previously described⁷. Micronuclei in NIH3T3 cells were quantified in cells fixed 72 h after IR based on DAPI and H3K9me3 staining.

Antibodies. Primary antibodies used in *Drosophila* cells were: anti-actin (1:1,000, Abcam, ab8224); anti-\(\gamma H2Av\) (1:1,000, Rockland, 600-401-914); anti-Rad51 (1:1,000, gift from J. Kadonaga); anti-HA (1:1,000, Abcam, ab9134 for western blot; 1:1,000; Covance, 16B12 for immunofluorescence); anti-Flag (1:1,000, Sigma, F1804); anti-GFP (1:1,000, Invitrogen, AP11122 for western blot; 1:1,000 Aves Laboratory, GFP-1020 for immunofluorescence; Rockland, 600-101-215 for immunoprecipitation); anti-H3K9me2 (1:750, Wako Chemicals, MABI0307, 302-32369); anti-Wash (1:10, Developmental Studies Hybridoma Bank, P3H3⁶⁷); anti-Wasp (1:5, Developmental Studies Hybridoma Bank, P5E1⁶⁸); anti-Scar (1:10, Developmental Studies Hybridoma Bank, P1C1⁶⁸); anti-Whamy (1:10, Developmental Studies Hybridoma Bank, P1D1⁶⁸); anti-Arpc3A (1:10,000, for western blotting, gift from L. Cooley), anti-Arpc3B (1:500, for immunofluorescence, gift from L. Cooley), anti-MyoV (head) (1:500, gift from A. Eprussi), anti-Unc45 (1:500, gift from S. Bernstein), anti-Smc5 (SDI, 1:800, gift from G. Karpen⁵); anti-Smc6; (SDI, 1:800, gift from G. Karpen⁵); anti-Nup62 (1:1,000, gift from H. Ohkura); anti-Rad50 (1:1,000, gift from M. Gatti), anti-dPIAS (1:1,000, gift from G. Karpen), anti-TopBP1 (1:1,000, gift from M. Michael⁶⁹); anti-HP1a (1:500, Developmental Studies Hybridoma Bank, C1A9⁷⁰). Primary antibodies used in NIH3T3 cells were: anti-H3K9me3 (1:2,000, Abcam, ab8898); anti pH3S10 (1:4,000, Milipore, 06-570); anti-\(\gamma H2AX \) (phospho-S139; 1:2,000, Abcam, ab26350). Secondary antibodies for immunofluorescence were from Life Technologies and Jackson Immunoresearch. Those used for western blotting were from Pierce and Santa Cruz Biotech. Antibodies were previously validated 5,7,44 or validated by comparing western blot or immunofluorescence signals in the presence of the protein of interest with signals after RNAi depletions, or immunofluorescence signals in the absence of primary antibodies.

Fly stocks and crosses. *Drosophila* were maintained on standard medium at 25 °C, which was prepared as previously described 71 . Stocks were obtained from BDSC (http://fly.bio.indiana.edu) or VDRC (https://stockcenter.vdrc. at/control/main) and are: Myo1A (BDSC #33971) y[1] sc[*] v[1]; P{y[+t7.7] v[+t1.8] = TRiP.HMS00298}attP2; Myo1B (BDSC #41689) y[1] v[1]; P{y[+t7.7] v[+t1.8] = TRiP.HMS02253}attP2; Arp3 (BDSC #32921) y[1] sc[*] v[1]; P{y[+t7.7] v[+t1.8] = TRiP.HMS00711}attP2; Wash (BDSC #62866) y[1] sc[*] v[1]; P{y[+t7.7] v[+t1.8] = TRiP.HMC05339}attP40; Scar (BDSC #31126) y[1] v[1]; P{y[+t7.7] v[+t1.8] = TRiP.JF01599}attP2; Act5c-GAL4 (BDSC #4414) y[1] w[*]; P{w[+mC] = Act5C-GAL4}25F01/CyO, y[+]; Unc45 (VDRC #v108868) P{KK101311}VIE-260B. The Smc5 trans-heterozygous mutant in Fig. 5f and

Extended Data Fig. 8i was $smc5^{7/19}$, previously described⁷. The wild-type control was w^{1118} . To obtain third instar larvae for karyotyping of neuroblast metaphase spread, RNAi lines were crossed to the Act5c–GAL4 line (balanced with CyO–GFP) and non-GFP larvae were picked for karyotyping as previously described⁷.

Statistics and reproducibility. All statistical analyses were performed using Prism 6 software (Graphpad), using the statistical tests indicated in the individual figure legends. Detailed information about sample sizes across different replicates and P values are provided as Source Data. No statistical methods were used to predetermine sample size. The experiments were not randomized and the investigators were not blinded to allocation during experiments and outcome assessment.

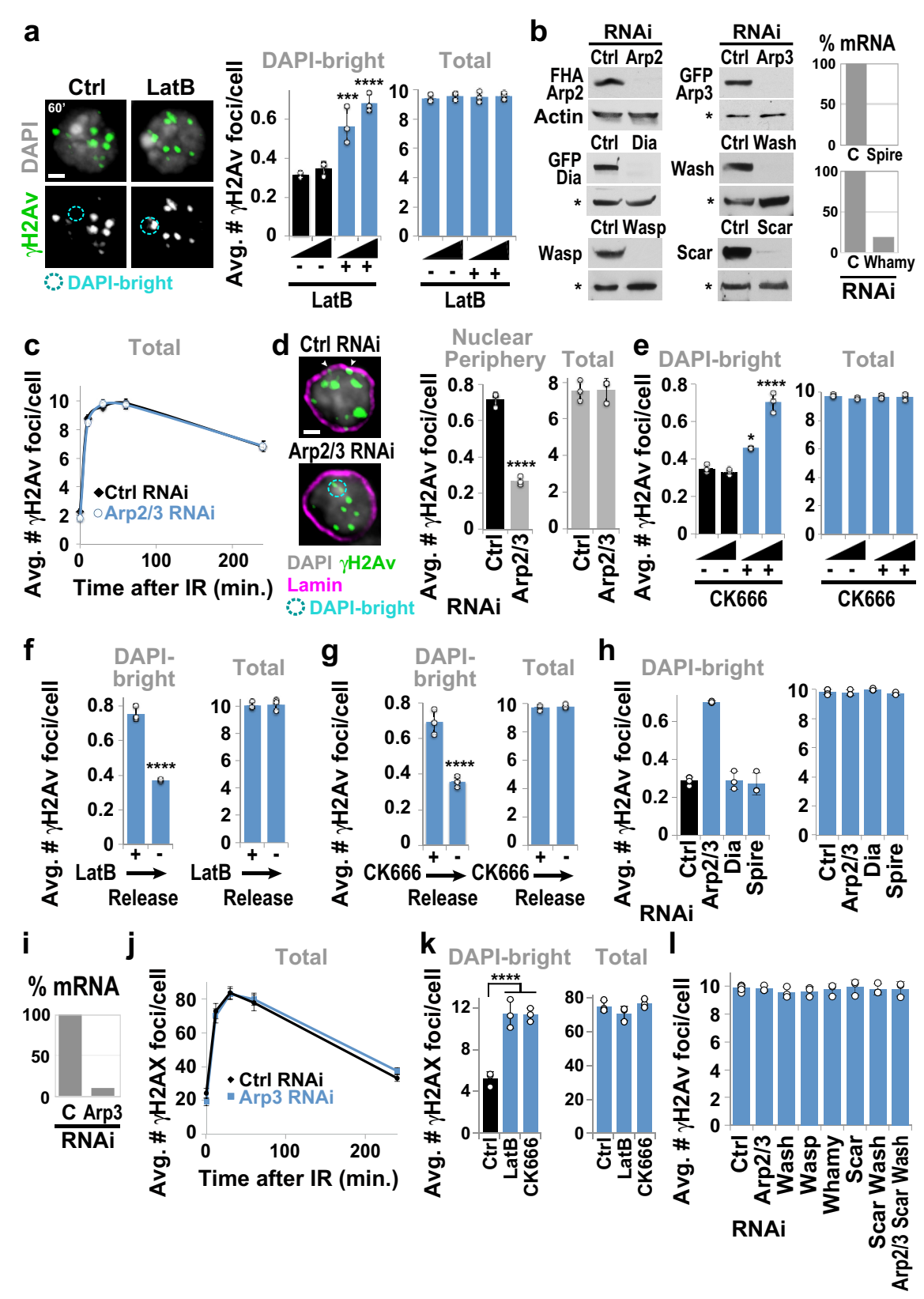
Reporting summary. Further information on experimental design is available in the Nature Research Reporting Summary linked to this paper.

 $\label{eq:code} \textbf{Code availability.} \ Custom \ scripts \ written \ in \ Matlab \ and \ R \ for \ image \ analysis \ have \ been \ published^{24}.$

Data availability. All relevant data are included in the main manuscript and figures, Extended Data and Supplementary Information. Additional data are available from the corresponding author upon reasonable request.

- 43. Cherbas, L. & Gong, L. Cell lines. Methods 68, 74-81 (2014).
- 44. Goodarzi, A. A., Noon, A. T. & Jeggo, P. A. The impact of heterochromatin on DSB repair. *Biochem. Soc. Trans.* **37**, 569–576 (2009).
- Noon, A. T. et al. 53BP1-dependent robust localized KAP-1 phosphorylation is essential for heterochromatic DNA double-strand break repair. *Nat. Cell Biol.* 12, 177–184 (2010).
- Erhardt, S. et al. Genome-wide analysis reveals a cell cycle-dependent mechanism controlling centromere propagation. J. Cell Biol. 183, 805–818 (2008).
- Hudson, A. M. & Cooley, L. A subset of dynamic actin rearrangements in Drosophila requires the Arp2/3 complex. J. Cell Biol. 156, 677–687 (2002).
- 48. Lee, C. F., Melkani, G. C. & Bernstein, S. I. The UNC-45 myosin chaperone: from worms to flies to vertebrates. *Int. Rev. Cell Mol. Biol.* **313**, 103–144 (2014).
- Kokai, E. et al. Analysis of nuclear actin by overexpression of wild-type and actin mutant proteins. *Histochem. Cell Biol.* 141, 123–135 (2014).
- Plessner, M., Melak, M., Chinchilla, P., Baarlink, C. & Grosse, R. Nuclear F-actin formation and reorganization upon cell spreading. *J. Biol. Chem.* 290, 11209–11216 (2015).
- Krauss, J., López de Quinto, S., Nüsslein-Volhard, C. & Ephrussi, A. Myosin-V regulates oskar mRNA localization in the *Drosophila* oocyte. *Curr. Biol.* 19, 1058–1063 (2009).
- Cheeseman, I. M. & Desai, A. A combined approach for the localization and tandem affinity purification of protein complexes from metazoans. Sci. STKE 2005, pl1 (2005).
- Verboon, J. M., Sugumar, B. & Parkhurst, S. M. Wiskott-Aldrich syndrome proteins in the nucleus: aWASH with possibilities. *Nucleus* 6, 349–359 (2015).
- 54. Verboon, J. M. et al. Wash interacts with lamin and affects global nuclear organization. *Curr. Biol.* **25**, 804–810 (2015).
- Larracuente, A. M. & Ferree, P. M. Simple method for fluorescence DNA in situ hybridization to squashed chromosomes. J. Vis. Exp. 95, 52288 (2015).
- Small, J. V., Herzog, M. & Anderson, K. Actin filament organization in the fish keratocyte lamellipodium. J. Cell Biol. 129, 1275–1286 (1995).

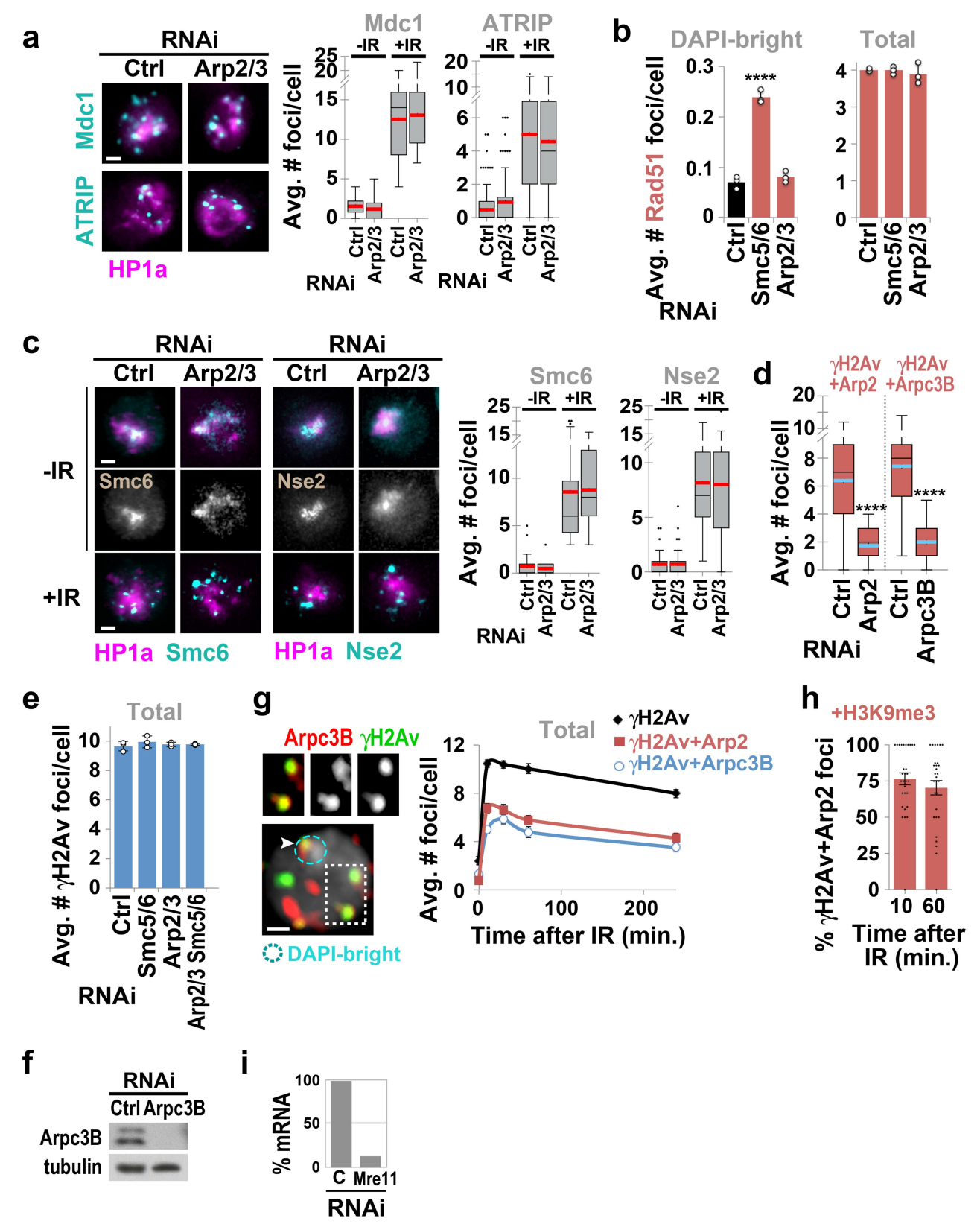
- 57. Sawasdichai, A., Chen, H. T., Abdul Hamid, N., Jayaraman, P. S. & Gaston, K. In situ subcellular fractionation of adherent and non-adherent mammalian cells. *J. Vis. Exp.* **41**, 1958 (2010).
- 58. Whelan, D. R. & Bell, T. D. Image artifacts in single molecule localization microscopy: why optimization of sample preparation protocols matters. *Sci. Rep.* **5**, 7924 (2015).
- Pierobon, P. et al. Velocity, processivity, and individual steps of single myosin V molecules in live cells. *Biophys. J.* 96, 4268–4275 (2009).
- Leyton Puig, D. et al. Tips and tricks for artifact-free PFA-based fixation of the actin cytoskeleton and its regulatory proteins for single molecule localization super-resolution microscopy. *Protoc. Exch.* (2016).
- 61. Baarlink, C., Wang, H. & Grosse, R. Nuclear actin network assembly by formins regulates the SRF coactivator MAL. *Science* **340**, 864–867 (2013).
- Yarrow, J. C., Lechler, T., Li, R. & Mitchison, T. J. Rapid de-localization of actin leading edge components with BDM treatment. BMC Cell Biol. 4, 5 (2003).
- Islam, K. et al. A myosin V inhibitor based on privileged chemical scaffolds. Angew. Chem. 49, 8484–8488 (2010).
- Angew. Chem. 49, 8484–8488 (2010).
 Nolen, B. J. et al. Characterization of two classes of small molecule inhibitors of Arp2/3 complex. Nature 460, 1031–1034 (2009).
- Belin, B. J., Cimini, B. A., Blackburn, E. H. & Mullins, R. D. Visualization of actin filaments and monomers in somatic cell nuclei. *Mol. Biol. Cell* 24, 982–994 (2013).
- Strober, W. Trypan blue exclusion test of cell viability. Curr. Protoc. Immunol. 111, A3.B.1–A3.B.3 (2015).
- Liu, R. et al. Wash functions downstream of Rho and links linear and branched actin nucleation factors. *Development* 136, 2849–2860 (2009).
- Rodriguez-Mesa, E., Abreu-Blanco, M. T., Rosales-Nieves, A. E. & Parkhurst, S. M. Developmental expression of *Drosophila* Wiskott–Aldrich Syndrome family proteins. *Dev Dyn.* 241, 608–626 (2012).
- Van Hatten, R. Á. et al. The Xenopus Xmus101 protein is required for the recruitment of Cdc45 to origins of DNA replication. J. Cell Biol. 159, 541–547 (2002).
- James, T. C. & Elgin, S. C. Identification of a nonhistone chromosomal protein associated with heterochromatin in *Drosophila melanogaster* and its gene. *Mol. Cell. Biol.* 6, 3862–3872 (1986).
- Ren, C., Webster, P., Finkel, S. E. & Tower, J. Increased internal and external bacterial load during *Drosophila* aging without life-span trade-off. *Cell Metab.* 6, 144–152 (2007).
- 72. Quinlan, M. E., Heuser, J. E., Kerkhoff, E. & Mullins, R. D. *Drosophila* Spire is an actin nucleation factor. *Nature* **433**, 382–388 (2005).
- Afshar, K., Stuart, B. & Wasserman, S. A. Functional analysis of the *Drosophila* diaphanous FH protein in early embryonic development. *Development* 127, 1887–1897 (2000).
- Melak, M., Plessner, M. & Grosse, R. Actin visualization at a glance. *J. Cell Sci.* 130, 525–530 (2017).
- Schoenenberger, C. A. et al. Conformation-specific antibodies reveal distinct actin structures in the nucleus and the cytoplasm. J. Struct. Biol. 152, 157–168 (2005).
- Dopie, J., Skarp, K. P., Rajakylä, E. K., Tanhuanpää, K. & Vartiainen, M. K. Active maintenance of nuclear actin by importin 9 supports transcription. *Proc. Natl Acad. Sci. USA* 109, E544–E552 (2012).
- Senaratne, T. N., Joyce, E. F., Nguyen, S. C. & Wu, C. T. Investigating the interplay between sister chromatid cohesion and homolog pairing in *Drosophila* nuclei. *PLoS Genet.* 12, e1006169 (2016).



Extended Data Fig. 1 | See next page for caption.

Extended Data Fig. 1 | Actin nucleators mediate relocalization of heterochromatic DSBs. a, Immunofluorescence and quantification of γ H2Av foci in DAPI-bright heterochromatin (dashed circle), or total focus number, of Kc cells fixed 60 min after IR after treatment with LatB (+) or control (Ctrl, -). ****P < 0.0001, ***P = 0.0008 versus control, n > 300 cells per treatment. b, Western blotting or qPCR analyses show RNAi depletion efficiencies for indicated proteins in Kc cells. Actin or a background band (*) were used as loading controls. c, Quantification of total γ H2Av foci from Fig. 1a. d, Immunofluorescence and quantification of γ H2Av foci at the nuclear periphery (Lamin), or total focus number, 60 min after IR after indicated RNAi depletions in Kc cells. Only middle z stacks were used for quantifications, as previously described *****P < 0.0001, n > 200 cells per RNAi. e, As in a but for cells treated with CK666. *****P < 0.0001, *P = 0.0293, *n > 300 cells per treatment. f, g, Quantification of γ H2Av foci in DAPI-bright heterochromatin or

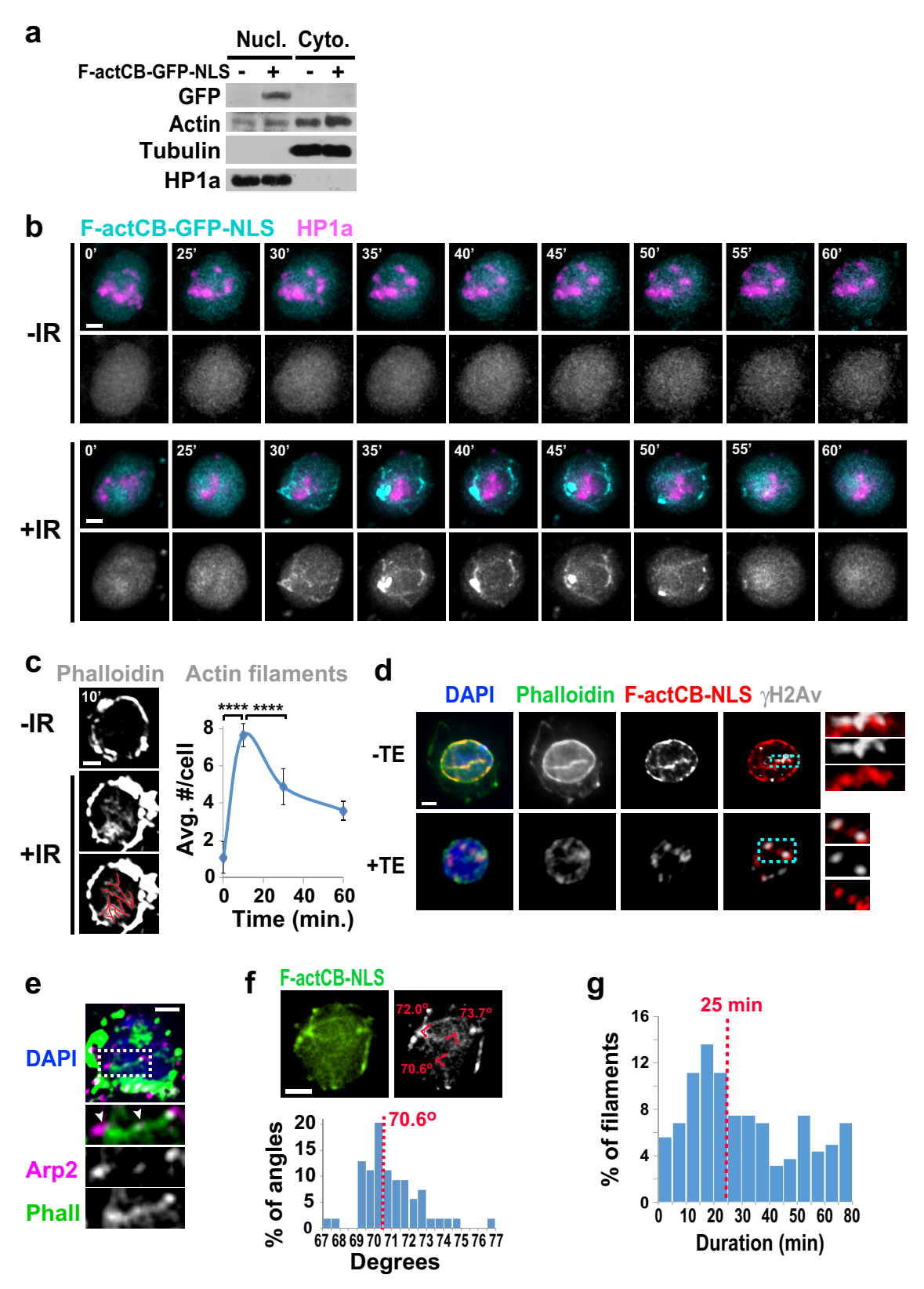
total focus number, after 60 min treatment with, and release from, LatB or CK666. *****P < 0.0001, n > 200 cells per condition. **h**, Quantification of γ H2Av foci in DAPI-bright heterochromatin, or total focus number, in Kc cells fixed 60 min after IR, after RNAi depletion of actin nucleators Spire⁷² or the formin Dia⁷³. ****P < 0.0001 versus control, n > 300 cells per RNAi. **i**, qPCR analysis shows ARP3 RNAi depletion efficiency in NIH3T3 cells. **j**, Quantification of total γ H2AX foci for Fig. 1b. **k**, Quantification of γ H2AX foci in DAPI-bright heterochromatin, or total focus number, in NIH3T3 G2 cells treated with indicated chemicals, and fixed 60 min after IR. ****P < 0.0001 versus control, n > 37 cells per treatment. **l**, Quantification of total γ H2Av foci for Fig. 1c. Scale bars, 1 μ m. Data shown as mean \pm s.e.m. in **c**, **j** and mean \pm s.d. of at least three independent experiments in **a**, **d**-**h**, **k**, **l**. P values calculated using two-tailed Mann–Whitney test.



Extended Data Fig. 2 | See next page for caption.

Extended Data Fig. 2 | Actin nucleators mediate relocalization of heterochromatic DSBs. a, Images 10 min after IR and quantification before (—) and 10 min after (+) IR of Mdc1 and Atrip foci in cells expressing GFP–Mdc1 or GFP–Atrip and mCherry–HP1a, after indicated RNAi depletions. $n \geq 48$ cells for Atrip; $n \geq 21$ cells for Mdc1. b, Quantification of Rad51 foci in cells fixed 60 min after IR and processed for immunofluorescence with anti-Rad51 antibodies after indicated RNAi depletions. Average number of foci shown relative to DAPI-bright or total foci. Smc5/6 RNAi results in abnormal formation of Rad51 foci in heterochromatin 5.7.8, and is used as positive control. ****P < 0.0001 versus control, unpaired t-test with Welch's correction, n > 300 cells per RNAi. c, Images and quantifications of Smc6 and Nse2 colocalizing with the HP1a domain before (—) IR and forming foci before and 15 min after (+) IR in cells expressing GFP–Smc6 or GFP–Nse2 and mCherry–HP1a

after indicated RNAi depletions. n=35 cells for Nse2 and $n\geq 23$ cells for Smc6. **d**, Quantification 30 min after IR of γ H2Av foci colocalizing with FHA-tagged Arp2 or with Arpc3B after indicated RNAi depletions. ****P<0.0001, two-tailed Mann–Whitney test, $n\geq 31$ cells per RNAi. **e**, Quantification of total foci for Fig. 1d. **f**, Western blot analyses show RNAi depletion efficiency for Arpc3B, and specificity of anti-Arp3cB antibodies. Tubulin is used as loading control. **g**, Immunofluorescence of γ H2Av foci colocalizing with Arpc3B and quantification of total focus number for Fig. 1f. **h**, Quantification at indicated times after IR of the percentage of γ H2Av foci colocalizing with FHA-Arp2 relative to H3K9me3 n=30. **i**, qPCR analysis shows Mre11 RNAi efficiency. Scale bars, 1 µm. Data shown as mean \pm s.e.m. in **a**, **c**, **d**, **g**, **h** and mean \pm s.d. of at least three independent experiments in **b**, **e**.



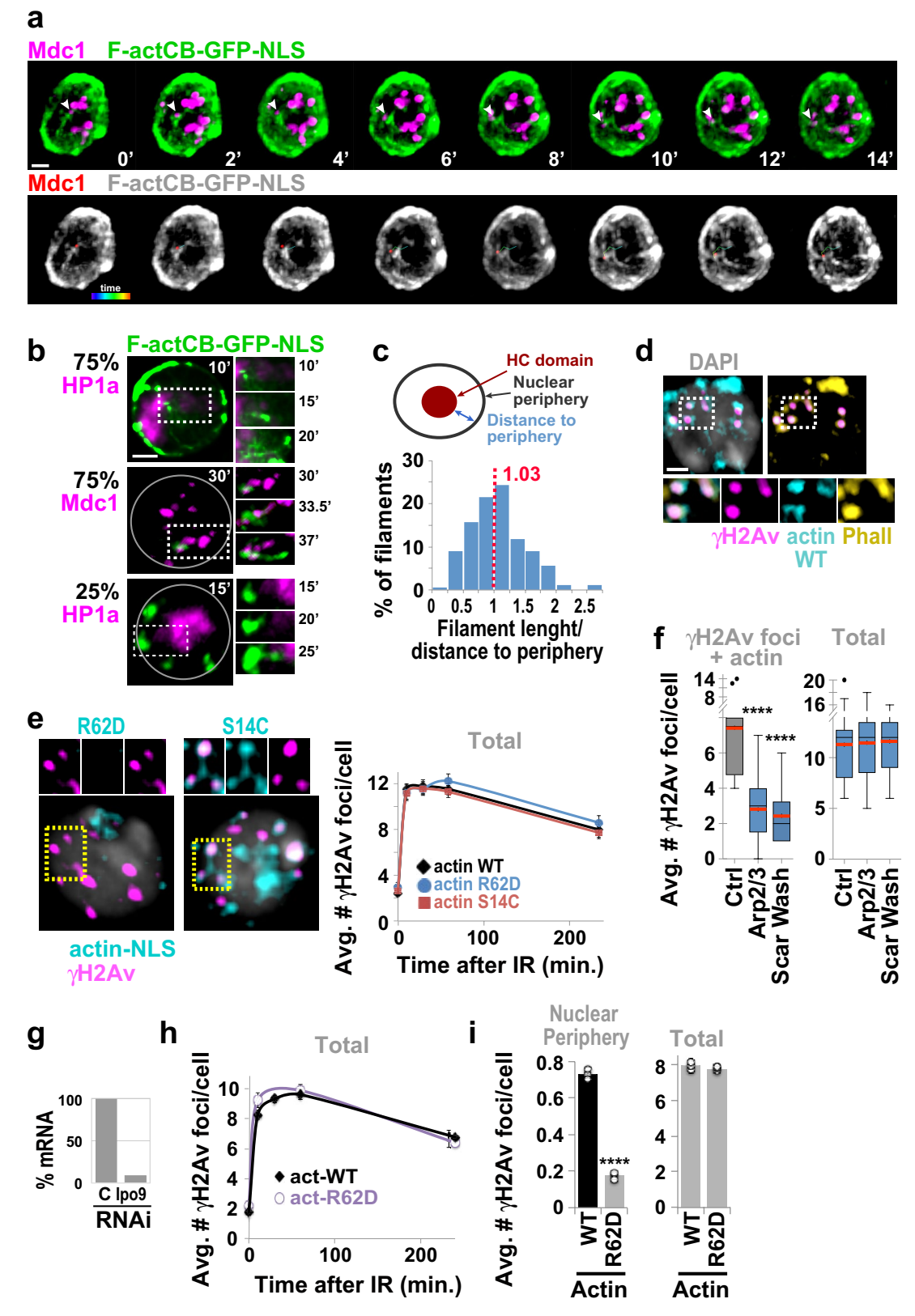
Extended Data Fig. 3 | See next page for caption.



Extended Data Fig. 3 | Nuclear F-actin is required for relocalization.

a, Western blot showing nuclear and cytoplasmic actin levels in cells stably transfected with F-actCB–GFP–NLS. HP1a and tubulin were used as loading controls and to check for purity of the fractions. Consistent with previous studies, expression of F-actCB–GFP–NLS does not alter nuclear actin levels 50,74 , providing a non-invasive method for nuclear actin detection in vivo. b, Frames of time-lapse experiments (Fig. 2a, Supplementary Videos 1, 2) of cells expressing F-actCB–GFP–NLS and mCherry–HP1a signals treated (+) or not treated (-) with IR. Time points are from IR (+IR Video) or the start of imaging (-IR Video). c, Immunofluorescence and quantification of cells stained with phalloidin show the formation of canonical nuclear actin filaments 75 (highlighted in red) at indicated time points after IR. ****P < 0.0001 for 10 min versus 0 min or 30 min, two-tailed Mann–Whitney test, $n \geq 51$ cells per time

point. Error bars show s.d. of at least three independent experiments. **d**, Immunofluorescence and staining for GFP, phalloidin, and γ H2Av, of cells expressing F-actCB–GFP–NLS, show examples of actin filaments coated with damage foci in the absence (—) of triton extraction (TE), and actin puncta colocalizing with γ H2Av foci after (+) TE. Zoomed details highlight colocalizations. **e**, Immunofluorescence and staining for HA and phalloidin (Phall) of cells expressing FHA–Arp2 show enrichment of Arp2 along nuclear actin filaments, including at the base of actin branches (arrowheads). **f**, Measurement of F-actin branch angles in response to IR, in time-lapse experiments with cells expressing F-actCB–GFP–NLS. n=54 angles. **g**, Quantification of the average duration of IR-induced actin filaments in time-lapse experiments with cells expressing F-actCB–GFP–NLS. n=162 actin filaments. Dashed red lines indicate median values in **f**, **g**. Scale bars, 1 μ m.

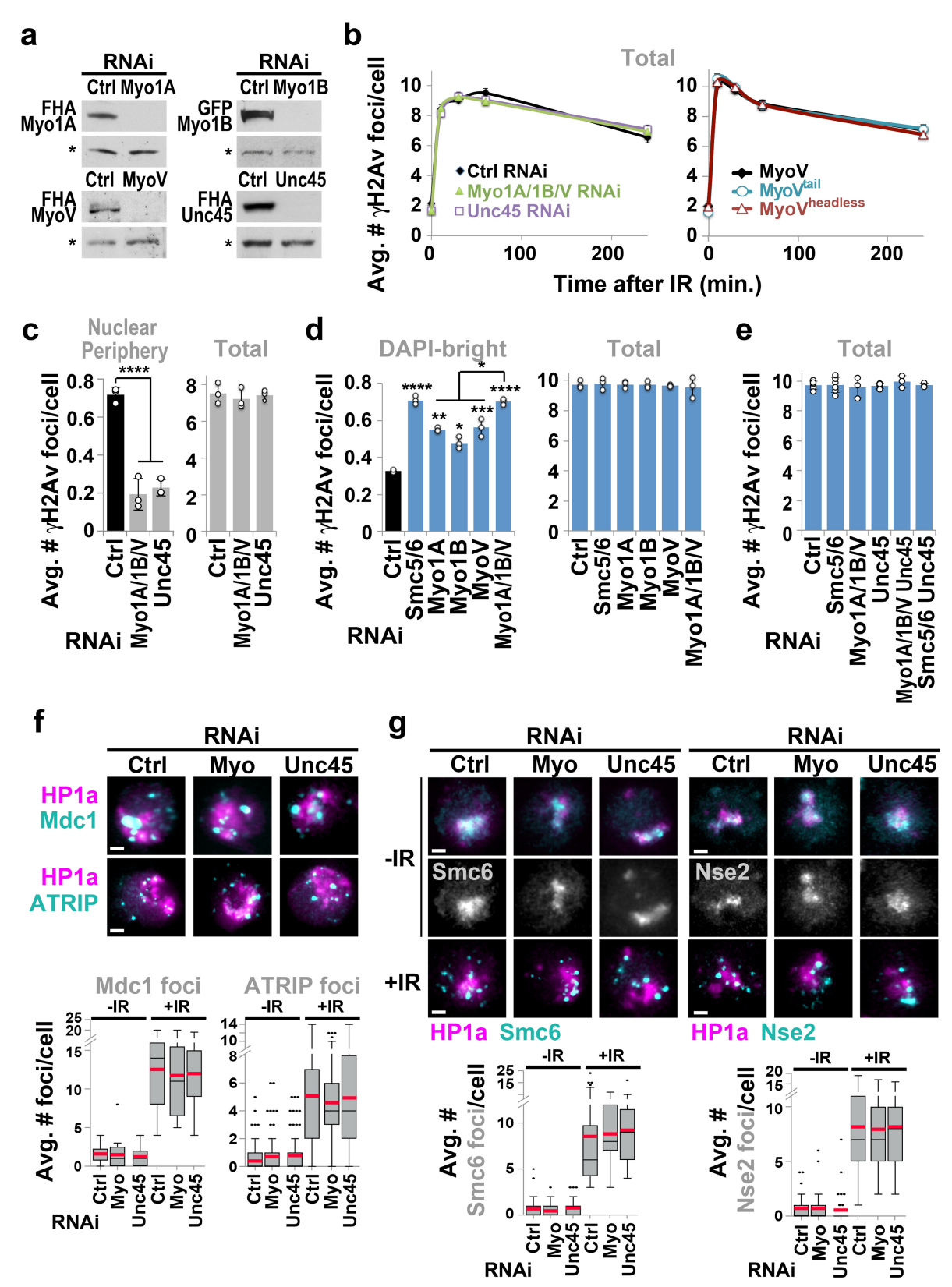


Extended Data Fig. 4 | See next page for caption.

Extended Data Fig. 4 | Nuclear F-actin is required for relocalization.

a, Frames from time-lapse experiment show cells expressing F-actCB-GFP-NLS and Mdc1-mCherry (Fig. 2c, Supplementary Video 3) with an example of a Mdc1 focus moving along an actin filament. Time indicates minutes from beginning of focus movement along the filament. Mdc1 focus tracking (bottom panels) was done in Imaris. b, Selected frames from cells expressing F-actCB-GFP-NLS and Mdc1-mCherry or HP1amCherry show examples of filament directionality at indicated time points after IR, that is, filaments emerging from the heterochromatin domain periphery (top), from repair foci (middle) or from the nuclear periphery (bottom). Percentages indicate the frequency with which each behaviour is observed. $n \ge 44$ filaments. **c**, Quantification of the length of actin filaments departing from the heterochromatin domain relative to the average distance between the HP1a domain periphery and the nuclear periphery. n > 140 filaments. Dashed red vertical line shows median value. d, Immunofluorescence and staining for Flag (actin(WT)), phalloidin (Phall), and \(\gamma H2Av \), of cells expressing Flag-NLS-actin(WT), show

examples of actin signals in cells processed by triton extraction before fixation, 10 min after IR. Zoomed details highlight colocalizations. Scale bar, 1 μm. e, Immunofluorescence of cells expressing Flag-NLS-tagged versions of actin(R62D) and actin(S14C) shows colocalizations with γ H2Av foci. Quantification shows total γ H2Av foci for Fig. 2d. f, Quantification of \(\gamma H2Av \) foci colocalizing with Flag-NLS-actin (WT) 10 min after IR, or total number of foci, after indicated RNAi depletions. ****P< 0.0001, $n \ge 14$ cells and $n \ge 158$ foci per RNAi. **g**, qPCR analysis shows Ipo9 RNAi depletion efficiency. Ipo9 depletion specifically blocks the transfer of actin monomers to the nucleus 14,76. h, Quantification of total γ H2Av foci for Fig. 2e. i, Quantification of cells fixed 60 min after IR shows γ H2Av foci at the nuclear periphery (lamin), or total focus number, after expression of indicated actin forms. Only the middle z stack was used for quantifications. ****P < 0.0001, $n \ge 215$ cells per experiment. Error bars, s.e.m. in e, f, h and s.d. of three independent experiments in i. P values calculated with two-tailed Mann–Whitney test.



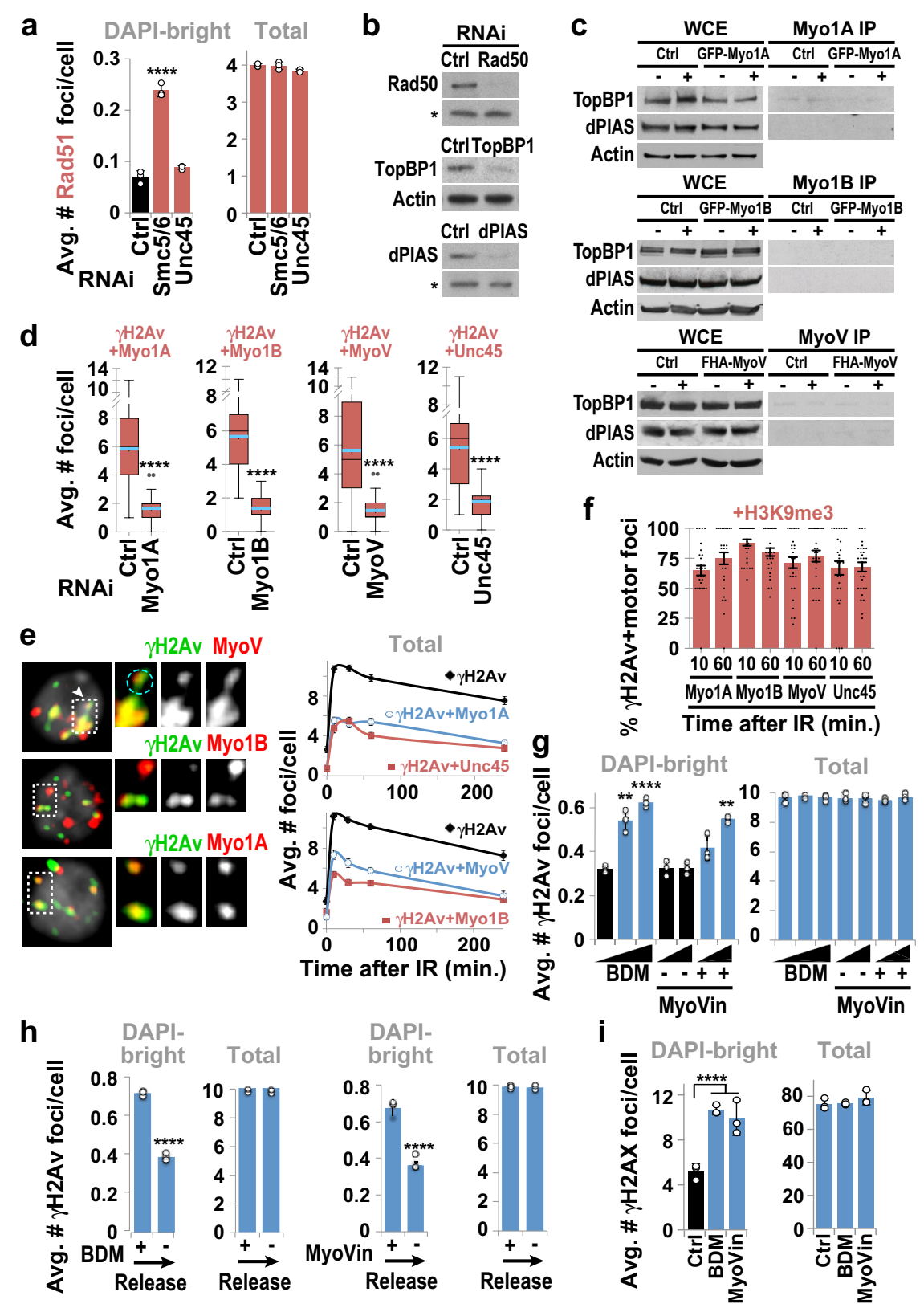
Extended Data Fig. 5 | See next page for caption.



Extended Data Fig. 5 | Relocalization relies on nuclear myosins.

a, Western blot analysis of cells expressing FHA-tagged components as indicated, shows RNAi depletion efficiency for indicated proteins. Background bands used as loading controls are indicated by an asterisk. **b**, Quantification shows total γ H2Av foci for Fig. 3a. **c**, Quantification of γ H2Av foci at the nuclear periphery (lamin) or total focus number in cells fixed 60 min after IR, after indicated RNAi depletions. ****P < 0.0001 versus control, $n \ge 200$ cells per RNAi. Only the middle Z-stack was used for quantifications. Control RNAi as in Extended Data Fig. 1d. **d**, Quantification of γ H2Av foci in DAPI-bright heterochromatin, or total focus number, in cells fixed 60 min after IR, after indicated RNAi depletions. ****P < 0.0001, ***P = 0.003, **P = 0.0022, * $P \le 0.0402$ versus control, $n \ge 200$ cells per RNAi. **e**, Quantification of total γ H2Av

foci for Fig. 3b. **f**, Images 10 min after IR and quantification at 0 (–IR) and 10 min after (+) IR of Mdc1 and Atrip foci in cells expressing GFP–Mdc1 or GFP–Atrip and mCherry–HP1a, after indicated RNAi depletions. $n \geq 75$ cells for Atrip and $n \geq 17$ cells for Mdc1. **g**, Images and quantifications of Smc6 and Nse2 colocalizing with the mCherry–HP1a domain before (–) IR and forming foci at 0 and 15 min after (+) IR in cells expressing GFP–Smc6 or GFP–Nse2 and mCherry–HP1a after indicated RNAi depletions. $n \geq 31$ cells for Nse2 and $n \geq 21$ cells for Smc6. In **f**, **g**, Myo indicates RNAi depletion of Myo1A, Myo1B and MyoV. Scale bars, 1 μ m. Data shown as mean \pm s.e.m. in **b**, **f**, **g** and mean \pm s.d. of at least three independent experiments in **c**–**e**. All P values calculated with two-tailed Mann–Whitney test except one-tailed Mann–Whitney test was used for Myo1B RNAi in **d**.



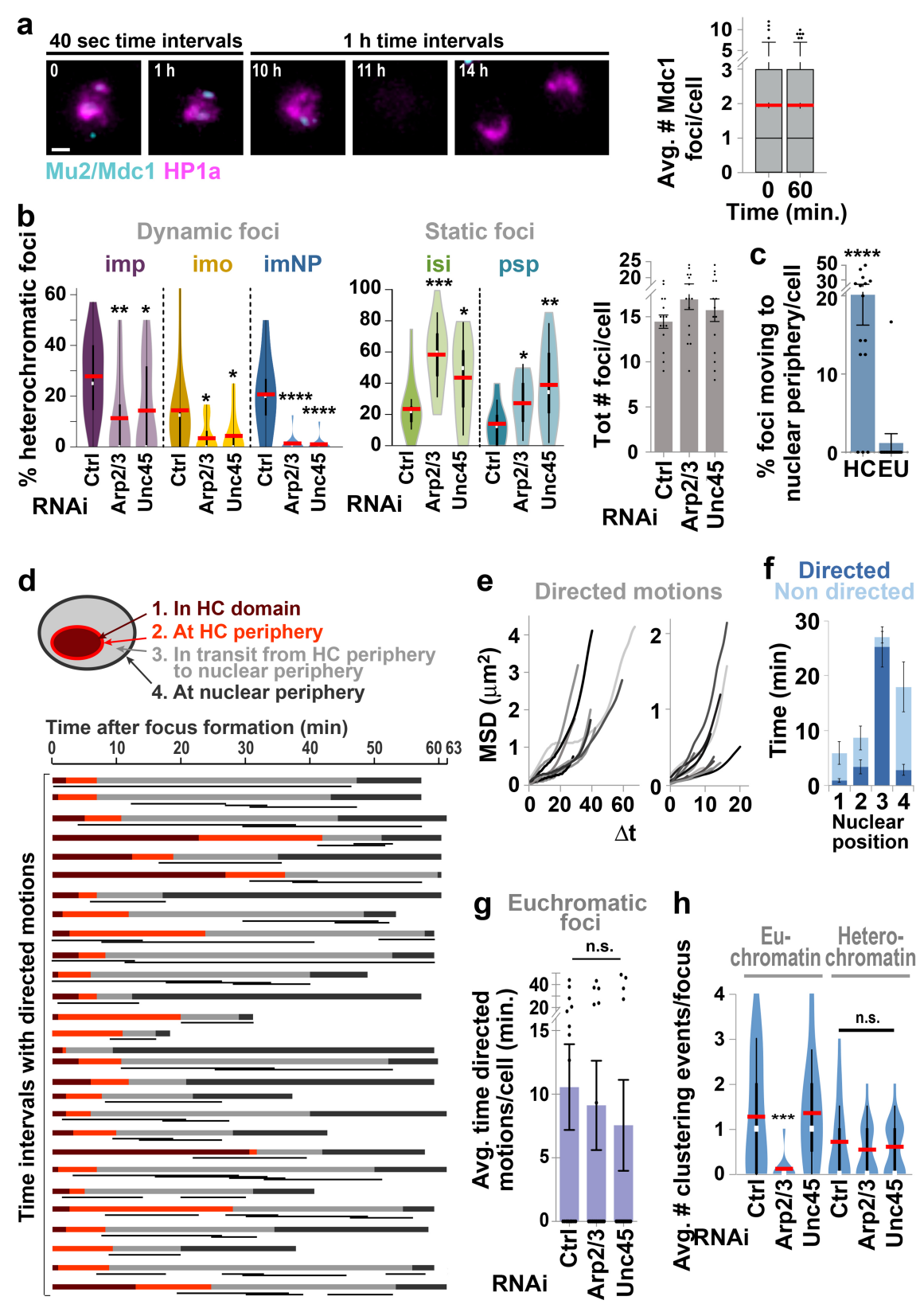
Extended Data Fig. 6 | See next page for caption.



Extended Data Fig. 6 | Relocalization relies on nuclear myosins.

a, Quantification of Rad51 foci in cells fixed 60 min after IR after indicated RNAi depletions shows the average number of foci relative to DAPI-bright heterochromatin or total foci. ****P = 0.0001 versus control, n > 300 cells per RNAi. Control and Smc5/6 RNAi as in Extended Data Fig. 2b. b, Western blot validation of the antibodies used in c and in Fig. 3c shows loss of Rad50, TopBP1 and dPIAS bands after corresponding RNAi depletions. c, Western blot analysis of the same immunoprecipitation shown in Fig. 3c probed with antibodies for dPIAS or TopBP1, with actin as the loading control. d, Quantification 30 min after IR of γ H2Av foci colocalizing with FHA–Myo1A, GFP–Myo1B, MyoV or Unc45 after indicated RNAi depletions. ****P < 0.0001, $n \ge 21$ cells per RNAi. e, Immunofluorescence 10 min after IR and quantification at indicated time points after IR of γ H2Av foci colocalizing with FHA–Myo1A,

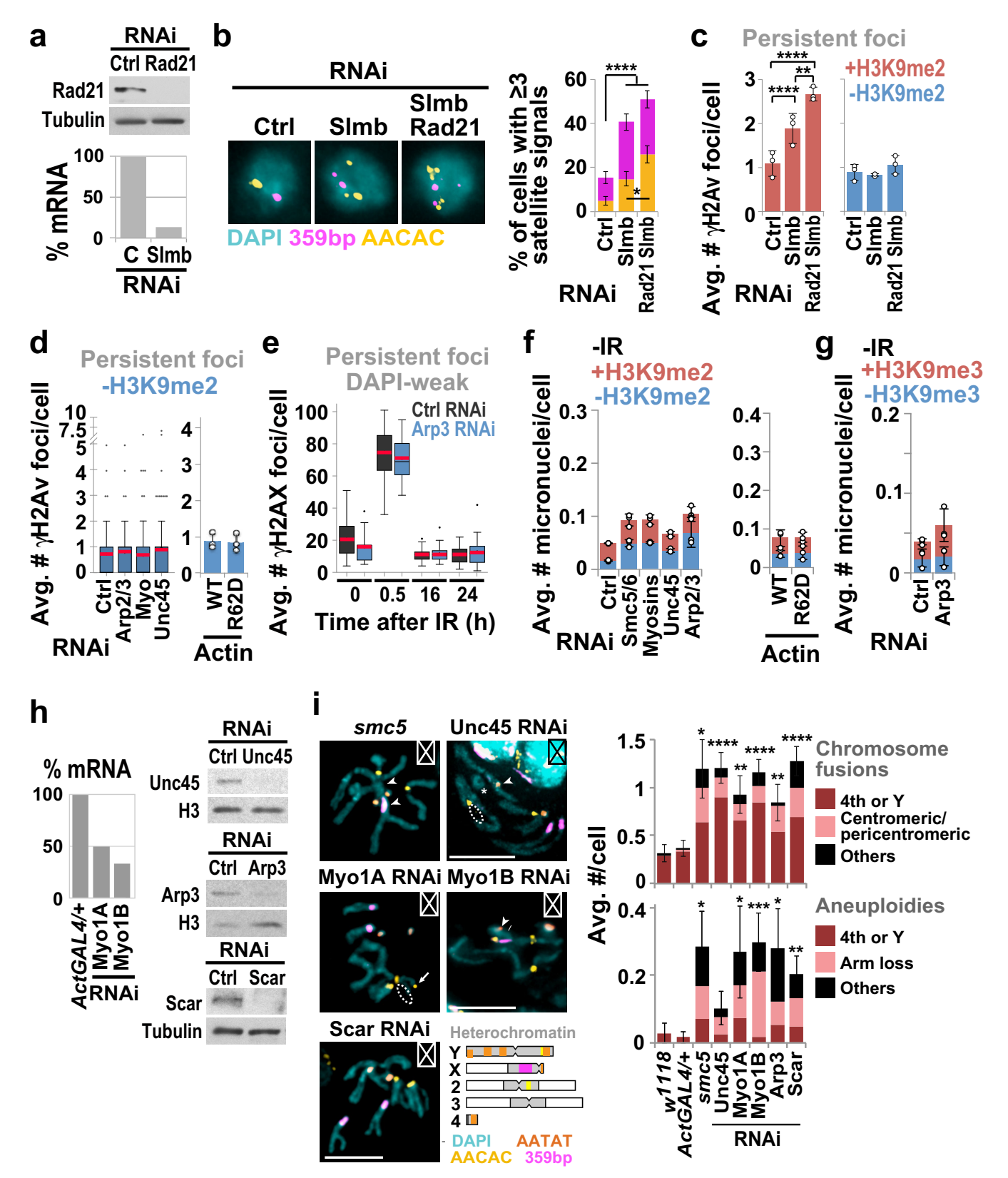
GFP–Myo1B, MyoV or Unc45. **f**, Quantification at indicated times after IR of the percentage of foci of γ H2Av + FHA–Myo1A, GFP–Myo1B, MyoV or Unc45, colocalizing with H3K9me3. n=30 cells per experiment per time point. **g**, Quantification of Kc cells fixed 60 min after IR shows γ H2Av foci in DAPI-bright heterochromatin, or total focus number, after treatment with BDM, MyoVin or in controls. ****P < 0.0001, **P < 0.008, $n \ge 300$ cells per treatment. **h**, Quantification of γ H2Av foci in DAPI-bright heterochromatin or total foci, after 60 min treatment with and release from BDM or MyoVin. ****P < 0.0001, $n \ge 190$ Kc cells per treatment. **i**, As in **g**, except NIH3T3 cells were used and γ H2AX foci were quantified. Control RNAi as in Extended Data Fig. 1k. ****P < 0.0001, $n \ge 37$ cells and $n \ge 2,760$ foci per treatment. Data shown as mean \pm s.e.m. in **d-f** and mean \pm s.d. of at least three independent experiments in **a**, **g-i**. All P values calculated with two-tailed Mann–Whitney test.



Extended Data Fig. 7 | See next page for caption.

Extended Data Fig. 7 | Actin nucleators and myosin drive directed motions of heterochromatic DSBs. a, Selected images and quantification at indicated time points of Mdc1 foci in cells expressing GFP-Mdc1 and mCherry-HP1a show no effect of the imaging conditions used in Fig. 4 on the ability of cells to divide or the total number of repair foci. Only representative time points are shown. n = 82 cells. Scale bar, 1 μ m. **b**, Left and middle, quantification and violin plot display of the frequency of heterochromatic Mdc1 foci moving relative to the HP1a domain during the time-lapse experiments shown in Fig. 4, after indicated RNAi depletions. White box, median; red line, mean; vertical black lines, values that occur 95% and 50% of the time. 'Dynamic HC foci' include foci moving from inside the HP1a domain to: the nuclear periphery (imNP); outside the HP1a domain (imo); or the periphery of the HP1a domain (imp). 'Static HC foci' include foci remaining inside (isi) or at the periphery of the HP1a domain (psp) throughout the 1-h timecourse. Colours reflect the categories analysed in Fig. 4b. Right, quantification of the average number of Mdc1 foci from Fig. 4a-d and b, after indicated RNAi depletions. *P < 0.05, **P < 0.006, ***P = 0.0002; ****P < 0.0001, two-tailed Mann–Whitney test, $n \ge 217$ foci per RNAi. c, Quantification

of the percentage of heterochromatic (HC) and euchromatic (EU) Mdc1 foci moving to the nuclear periphery in time-lapse experiments from Fig. 4a. ****P < 0.0001; two-tailed Mann–Whitney test, n > 57 foci. d, LDM analysis of Mdc1 foci that reach the nuclear periphery from Fig. 4b. Each coloured horizontal bar represents a focus and its duration in each nuclear compartment, as indicated. The black segments under each bar are LDMs for each focus. n = 28 foci. **e**, MSD curves generated from the positional data corresponding to the time points that contain LDMs in **d**. Longer (left) and shorter (right) LDMs are presented as independent graphs for clarity. f, Quantification of the analysis shown in Fig. 4c and d shows the average duration of directed motions (LDMs) or non-directed motions in the nuclear locations defined in **d**. P < 0.0001 for directed motions in 3 versus 1, 2, 4, unpaired *t*-test. **g**, Quantification of LDM durations for euchromatic foci shown in Fig. 4d, after indicated RNAi depletions. h, Quantification and violin plot of Mdc1 focus clustering events in time-lapse experiments for Fig. 4d. Graphical display as in b. An example of clustering is highlighted in Supplementary Video 4. ***P = 0.0003, two-tailed Mann–Whitney test, $n \ge 20$ cells per RNAi. Error bars, s.e.m in a, b (right graph), c, f, g.



Extended Data Fig. 8 | See next page for caption.

Extended Data Fig. 8 | Actin nucleators and myosins promote heterochromatin repair and stability. a, Western blotting and qPCR analysis show RNAi depletion efficiency for Rad21 and Slmb as indicated. Tubulin is a loading control. b, FISH analysis and quantification show the effect of indicated RNAi on the number of cells with ≥ 3 AACAC or 359bp satellites, reflecting disruption of homologous and/or sister pairing⁷⁷. **P = 0.0472; ****P < 0.0001, two-tailed Mann–Whitney test, n > 120 cells per RNAi. c, Quantification shows γ H2Av foci associated (+) or not associated (-) with H3K9me2 signals 20 h after IR following indicated RNAi depletions. **P = 0.0015; ****P < 0.0001, two-tailed Mann–Whitney test, n > 420 cells per RNAi. d, Quantification of Kc cells from the experiment in Fig. 5a shows γ H2Av foci not associated (-) with H3K9me2 signals 20 h after IR and following indicated RNAi depletions. e, Quantification of NIH3T3 cells from the experiment in Fig. 5b shows γ H2AX foci not associated (-) with DAPI-bright signals 16 and 24 h

after IR and following indicated RNAi depletions. **f**, Quantification of micronuclei in non-irradiated Kc cells from Fig. 5d. **g**, Quantification of micronuclei in non-irradiated NIH3T3 cells from Fig. 5e. **h**, qPCR and western blotting analyses show RNAi depletion efficiency of indicated components in third instar larvae for **i** and Fig. 5f. **i**, Images and quantification of chromosomal aberrations in karyotypes from Fig. 5f. Images show extra satellites (arrows), chromosome fusions (arrowhead) and chromosome arm losses (dashed circles). The diagram of *Drosophila* chromosomes indicates the positions of the main satellites detected by FISH. Aneuploidies and chromosome fusions from Fig. 5f were further categorized to highlight rearrangements involving centromeric regions or chromosomes that are predominantly heterochromatic (fourth or Y). ****P \leq 0.0001, **P \leq 0.0079, *P \leq 0.0433, unpaired *t*-test with Welsh correction. Error bars, s.e.m. in **b**, **d** (RNAi), **e**, **i** and s.d. of at least three independent experiments in **c**, **d** (actin), **f**, **g**.

natureresearch

Corresponding author(s):	Irene Chiolo	
Initial submission	Revised version	Final submission

Life Sciences Reporting Summary

Nature Research wishes to improve the reproducibility of the work that we publish. This form is intended for publication with all accepted life science papers and provides structure for consistency and transparency in reporting. Every life science submission will use this form; some list items might not apply to an individual manuscript, but all fields must be completed for clarity.

For further information on the points included in this form, see Reporting Life Sciences Research. For further information on Nature Research policies, including our data availability policy, see Authors & Referees and the Editorial Policy Checklist.

Experimental design

1. Sample size

Describe how sample size was determined.

We performed initial experiments to evaluate the variance of the population, and chose the sample size so that we have a 80% power of detecting a mean difference of 20% from the controls, with a significance level of 5% (two sided). GraphPad StatMate software was used for these estimates.

2. Data exclusions

Describe any data exclusions.

No samples were excluded. Within each fixed sample, dead cells and mitotic cells (identified by DAPI staining) were excluded. Cells that display excessive rotational/translational motions that could not be corrected for with our registration method, were excluded from the analysis of focus dynamics in movies.

3. Replication

Describe whether the experimental findings were reliably reproduced.

4. Randomization

Describe how samples/organisms/participants were allocated into experimental groups.

5. Blinding

Describe whether the investigators were blinded to group allocation during data collection and/or analysis.

The cells quantified in each experiment were randomly sampled from the total population of cells.

All the described findings were reliably reproduced.

We assured reliable and unbiased data quantification by having different investigators quantify each experiment independently. Analyses were done on randomized samples. No animals or human research participants were involved. Other levels of blinding are not relevant to this study.

Note: all studies involving animals and/or human research participants must disclose whether blinding and randomization were used.

6	Statistical	parameter
υ.	Statistical	Darameter

For all figures and tables that use statistical methods, confirm that the following items are present in relevant figure legends (or in the Methods section if additional space is needed).

n/a	Confirmed
	The exact sample size (n) for each experimental group/condition, given as a discrete number and unit of measurement (animals, litters, cultures, etc.)
	A description of how samples were collected, noting whether measurements were taken from distinct samples or whether the same sample was measured repeatedly
	A statement indicating how many times each experiment was replicated
	The statistical test(s) used and whether they are one- or two-sided (note: only common tests should be described solely by name; more complex techniques should be described in the Methods section)
	A description of any assumptions or corrections, such as an adjustment for multiple comparisons
	The test results (e.g. <i>P</i> values) given as exact values whenever possible and with confidence intervals noted
	A clear description of statistics including <u>central tendency</u> (e.g. median, mean) and <u>variation</u> (e.g. standard deviation, interquartile range)
	Clearly defined error bars

See the web collection on statistics for biologists for further resources and guidance.

▶ Software

Policy information about availability of computer code

7. Software

Describe the software used to analyze the data in this study.

Details are specified in the methods sections. The main software used for data analyses are SoftWorX (6.0), Matlab (R2013a), R (Version 0.98.978), and Imaris x64 (7.7.1). Two custom algorithms used for this study are now published in 'Methods in Enzymology' (Caridi et al., https://doi.org/10.1016/bs.mie.2017.11.033), and references have been updated accordingly.

For manuscripts utilizing custom algorithms or software that are central to the paper but not yet described in the published literature, software must be made available to editors and reviewers upon request. We strongly encourage code deposition in a community repository (e.g. GitHub). *Nature Methods* guidance for providing algorithms and software for publication provides further information on this topic.

Materials and reagents

Policy information about availability of materials

8. Materials availability

Indicate whether there are restrictions on availability of unique materials or if these materials are only available for distribution by a for-profit company.

All materials generated for this study are readily available from the authors or commercial sources specified in the Methods session.

9. Antibodies

Describe the antibodies used and how they were validated for use in the system under study (i.e. assay and species).

Primary antibodies used in Drosophila cells were: anti-actin (1:1000, Abcam, ab8224); anti-yH2Av (1:1000, Rockland, 600-401-914); anti-Rad51 (1:1000, gift from J. Kadonaga); anti-HA (1:1000, Abcam, ab9134 for Western blot; 1:1000; Covance, 16B12 for IF); anti-FLAG (1:1000, Sigma, F1804); anti-GFP (1:1000, Invitrogen, AP11122 for Western blot; 1:1000 Aves Lab, GFP-1020 for IF; Rockland, 600-101-215 for Ip); anti-H3K9me2 (1:750, Wako Chemicals, MABI0307, 302-32369); anti-Wash (1:10, Developmental Studies Hybridoma Bank, P3H3); anti-Wasp (1:5, Developmental Studies Hybridoma Bank, P5E1); anti-Scar (1:10, Developmental Studies Hybridoma Bank, P1C1); anti-Whamy (1:10, Developmental Studies Hybridoma Bank, P1D1); Phalloidin (1:500 AlexaFluor488, Invitrogen, A12379), anti-Arpc3A (1:10,000, for Wb kind gift from L. Cooley), anti-Arpc3B (1:500 for IF, kind gift from L. Cooley), anti-MyoV (head) (1:500, kind gift from A. Eprussi), anti-Unc45 (1:500, kind gift from S. Bernstein), anti-Smc5 (SDI, 1:800)3; anti-Smc6; (SDI, 1:800)3; anti-Nup62 (1:1000, kind gift from H. Ohkura); anti-Rad50 (1:1000, kind gift from M. Gatti), anti-dPIAS (1:1000, kind gift from G. Karpen), anti-TopBP1 (1:1000, kind gift from M. Michael36); anti-HP1a (1:500, Developmental Studies Hybridoma Bank, C1A9). Primary antibodies used in NIH3T3 cells were: anti-H3K9me3 (1:2000, Abcam, ab8898); anti pH3S10 (1:4000, Milipore, 06-570); anti-gamma H2A.X (phospho-S139; 1:2000, Abcam, ab26350). Secondary antibodies for IF were from Life Technologies and Jackson Immunoresearch. Those used for Western blot were from Pierce and Santa Cruz Biotech. Antibodies were previously validated 3,4,14 or validated by comparing signals in the presence of the protein of interest with signals after RNAi depletions or IF signals in the absence of primary antibodies.

10. Eukaryotic cell lines

a. State the source of each eukaryotic cell line used.

Kc167 (Kc) cells were used for most experiments and were purchased from the Drosophila Genomic Resource Center (DGRC). Mouse NIH3T3 cells were obtained from ATCC.

b. Describe the method of cell line authentication used.

Kc167 (Kc) cells were authenticated by DGRC, and mouse NIH3T3 cells by ATCC.

 Report whether the cell lines were tested for mycoplasma contamination. Cell lines were tested for micoplasma contamination and no contamination was found.

d. If any of the cell lines used are listed in the database of commonly misidentified cell lines maintained by ICLAC, provide a scientific rationale for their use.

No commonly misidentified cell lines were used in this study.

Animals and human research participants

Policy information about studies involving animals; when reporting animal research, follow the ARRIVE guidelines

11. Description of research animals

Provide details on animals and/or animal-derived materials used in the study.

Fly stocks were obtained from BDSC (http://fly.bio.indiana.edu) or VDRC (www.vdrc.at) and are: Myo1A (BDSC #33971) y[1] sc[*] v[1]; P{y[+t7.7] v[+t1.8]=TRiP.HMS00298}attP2; Myo1B (BDSC #41689) y[1] v[1]; P{y[+t7.7] v[+t1.8]=TRiP.HMS00213}attP2; Arp3 (BDSC #32921) y[1] sc[*] v[1]; P{y[+t7.7] v[+t1.8]=TRiP.HMS00711}attP2; Wash (BDSC #62866) y[1] sc[*] v[1]; P{y[+t7.7] v[+t1.8]=TRiP.HMC05339}attP40; Scar, (BDSC #31126) y[1]v[1]; P{y[+t7.7] v[+t1.8]=TRiP.JF01599}attP2; Act5c-GAL4 (BDSC #4414) y[1] w[*]; P{w[+mC]=Act5C-GAL4}25F01/CyO, y[+]; Unc45 (VDRC #v108868) P{KK101311}VIE-260B. Smc5 trans-heterozygous mutant was smc57/19 previously described in Chiolo et al, Cell, 2011 (doi:10.1016/j.cell.2011.02.012). The WT control was w1118 (http://flybase.org/reports/FBal0018186.html). To obtain 3rd instar larvae for karyotyping of neuroblast metaphase spread, RNAi lines were crossed to the Act5c-GAL4 line (rebalanced with CyO-GFP) and non-GFP larvae were picked for karyotyping as described in Chiolo et al, Cell, 2011 (doi:10.1016/j.cell.2011.02.012).

Policy information about studies involving human research participants

12. Description of human research participants

Describe the covariate-relevant population
characteristics of the human research participants.

The study did not involve human research participants.